EXPERIMENTAL INVESTIGATION OF BUBBLE LATERAL MOTION IN SHEAR FLOW

by

Ke Tang

A Thesis

Submitted to the Faculty of Purdue University

In Partial Fulfillment of the Requirements for the degree of

Master of Science in Nuclear Engineering

School of Nuclear Engineering

West Lafayette, Indiana

December 2018

THE PURDUE UNIVERSITY GRADUATE SCHOOL
STATEMENT OF COMMITTEE APPROVAL

Dr. Mamoru Ishii, Chair
School of Nuclear Engineering
Dr. Martin Lopez-De-Bertodano
School of Nuclear Engineering
Dr. Amy Marconnet
School of Mechanical Engineering

Approved by:

Dr. Seungjin Kim
Head of the Graduate Program

ACKNOWLEDGMENTS

The author would like to give his deepest gratitude to his advisor Professor Mamoru Ishii for providing the opportunity to work at Thermal-hydraulics and Reactor Safety Laboratory (TRSL) at Purdue University and guiding the research during master program period. The author would like to extend his thanks to his colleagues at TRSL, who gave many valuable suggestions to this work, especially Yang Zhao, Muhao Zhang and Qingzi Zhu for their collaborations and contributions.

In addition, the author would like to appreciate Professor Martin Lopes de Bertodano and Professor Amy Marconnet for being part of the committee and providing support and help.

Last but not least, the author would like to thank the endless love from his parents and the joy from his friends during the time of his master program study.

TABLE OF CONTENTS

LIST OF TABLES

LIST OF FIGURES

NONMENCLATURE

Latin Characters

a	Major axis of bubble [mm]
b	Minor axis of bubble [mm]
B_k	Volume [m^3]
C_L	Lift coefficient [-]
C_D	Drag coefficient [-]
d_e	Equivalent diameter [mm]
d_{fringe}	Distance between interfere fringes [m]
D_{sm}	Sauter mean diameter [mm]
E	Aspect ratio [-]
Eo	Eötvös number [-]
Eo_H	Modified Eötvös number [-]
F^D	Drag force [N]
F^V	Virtual mass force [N]
F^B	Buoyancy force [N]
F^L	Lift force [N]
F^W	Wall lift force [N]
F^T	Turbulent dispersion force [N]
F_L	Lift force [N]
L_o	Total lateral moving distance [mm]
m	Oscillation times [-]
M	Morton number [-]
M_k	Generalized drag force [N]
M^D	Generalized drag force [N]
M^V	Generalized virtual mass force [N]
M^B	Generalized buoyancy force [N]

M^L	Generalized lift force [N]
M^W	Generalized wall lift force [N]
M^T	Generalized turbulent dispersion force [N]
n	Frame number [-]
g	Gravity acceleration [m/s^2]
O_s	Average oscillation amplitude [mm]
r_p	Particle radius [m]
Re	Reynolds number
S	Projected bubble area [mm^2]
Sr	Non-dimension shear rate magnitude [-]
St	Strouhal number [-]
v_r	Relative velocity between liquid and gas [-]
V_T	Terminal velocity of bubble [mm/s]
Vs	Sedimentation velocity [m/s]
W	Width of the channel [mm]
We	Weber number [-]
x	Lateral position [mm]
y	Lateral position [mm]
z	Vertical position [mm]

Greek Characters

α	Void fraction [-]
ρ	Density [kg/m^3]
v	Velocity [m/s]
θ	Angle between bubble moving direction and vertical direction [°]
ε	Tuning factor for bubble terminal velocity prediction [-]
λ	Wavelength [m]
β	Angle between two laser beams [°]
μ	Viscosity [$Pa \cdot S$]

σ	Surface tension [N/m]
ω	Shear rate magnitude [s^{-1}]
ξ	Tuning factor of drag coefficient predficition
Δt	Time interval [s]
τ	Response time [s]

Subscripts/Superscripts

f	Liquid phase
g	Gas phase
k	k^{th} phase

Operators

∇	Gradient operator
$\nabla\cdot$	Divergence operator

ABSTRACT

Author: Tang, Ke. MSNE
Institution: Purdue University
Degree Received: December 2018
Title: Experimental Investigation of Bubble Lateral Motion in Shear Flow
Committee Chair: Mamoru Ishii

In two-phase flow, the void fraction and its distribution are two major factors describing the characteristic of flow patterns. Better understanding of void fraction distribution in two-phase flow would help improve safety and efficiency in the nuclear industry as the heat transfer process is significantly affected by the void distribution in nuclear reactor fuel bundles. Lift force is proposed to explain the lateral migration of bubbles in the shear flow (Feng & Bolotnov, 2017, Lucas & Tomiyama, 2011, Akio Tomiyama, Tamai, Zun, & Hosokawa, 2002). However, the mechanism of lift force is unclear and the research on lift force is limited.

An experimental investigation is performed on the lift force of single bubble in weak linear shear flow field in water. In addition, characteristics of bubble motion including bubble terminal velocity, aspect ratio and oscillation amplitude are studied and comparisons are made with existing models.

It was found that the model proposed by Tomiyama et al. (A. Tomiyama, Celata, Hosokawa, & Yoshida, 2002) has the best prediction of bubble terminal velocity with introduction of a tuning factor in consideration of the asymmetric deformation of bubble. Bubble aspect ratio is found to significantly affect its terminal velocity, and a new model is proposed to best fit the experiment data. It is also observed that the shear rate magnitude has no influence on bubble aspect ratio in this study. Oscillation was observed for all the bubbles in this experiment. Oscillation amplitude scattered widely and it was difficult to correlate it only with the bubble equivalent diameter. In terms of lift force, positive lift coefficient was observed for small size bubbles and transits to negative value with growing size. Due to the high Reynolds number of flow and low viscosity of water, widely scattered data is found in the results. Although the accurate prediction of lift coefficient is difficult to obtain in the experiment, the lift coefficient transition trend is given and

agrees with many other research. In addition, this research provides a database for further lift coefficient investigation.

CHAPTER 1. INTRODUCTION

1.1 Background

Characteristic of two-phase flow is important in many engineering systems like the oil industry, biological system, energy system, etc. Accurate prediction of the two-phase flow structure would benefit these industries such as improving the critical heat flux of the nuclear reactor fuel bundles.

Among all the models describing two-phase flow, the two-fluid model is the state of art model tacking the difficulty in this field by introducing interfacial area concentration. It was proposed by Ishii and Mishima in 1975 (Mamoru Ishii & Hibiki, 2010). Mass balance, momentum balance and energy balance are described by the field equations in this model and are the most important part in analyzing the two-phase flow. Among these field equations, momentum equation for each phase can be expressed as follows:

$$\frac{\partial \alpha_k \overline{\overline{\rho_k} v_k}}{\partial t} + \nabla \cdot (\alpha_k \overline{\overline{\rho_k} v_k v_k}) = -\nabla \left(\alpha_k \overline{\overline{p_k}} \right) + \nabla \cdot \left[\alpha_k \left(\overline{\overline{\tau_k}} + \tau_k^T \right) \right] + \alpha_k \overline{\overline{\rho_k}} g_k + M_k \tag{1.1}$$

The right side term M_k is the generalized interfacial drag force and can be expressed as:

$$\begin{aligned} M_k &= \frac{\alpha_k}{B_k} \left(F_k^D + F_k^V + F_k^B + F_k^L + F_k^W + F_k^T \right) \\ &= M_k^D + M_k^V + M_k^B + M_k^L + M_k^W + M_k^T \end{aligned} \tag{1.2}$$

where $B_k, F^D, F^V, F^B, F^L, F^W$ and F^T represent volume, the standard drag force, virtual mass force, the Basset force, the lift force, the wall lift force and turbulent dispersion force for a typical single particle, respectively.

Lift force is a major force governing the lateral migration of bubble in shear flow. It is generated by the relative velocity difference in the fluid or rotation of flow field. The direction of lift force is normal to the particle moving direction, which would govern bubble lateral motion behavior. Thus, it has great effect on lateral distribution of void fraction and interfacial area concentration. It was observed by Usui et al.(Usui & Sato, 1989) that in bubbly vertical downward flow, void fraction shows a peak between the pipe center and the wall. Serizawa et al. (Serizawa, Kataoka, & Michiyoshi, 1975) found that the distribution of void fraction in pipe flow is a strong function of

the flow pattern. Peaking phenomenon of the local void fraction was observed in the vicinity of the pipe wall in upward flow. Wang et al. also (Wang, Lee, Jones, & Lahey, 1987) mentioned that for downward flow, small bubbles tend to migrate to the center of the flow while for upward flow, small bubbles tend to migrate to the wall. This different phenomenon may be attributed to the interactions between the walls and bubbles. In addition, lift force has always been suggested as a potential reason to explain this phenomenon.

Proper modeling of lift force in the two-fluid model is of vital importance in nuclear engineering. Nuclear power safety would be improved with more information on void fraction distribution. However, the study of lift force, which affects the radial distribution of void fraction, remains a big challenge due to the difficulty of performing experiments in shear flow. Until now, many different theories and models were proposed to explain and predict the lift force acting on bubble in shear flow. Among them, the lift coefficient model proposed by Tomiyama et al. (Akio Tomiyama et al., 2002) has been widely used by other researches in code development. Because it was developed based on the high viscous fluid and only validate in low Reynolds number regime from 3.6 to 78. The validation of this model in low viscosity fluid and high Reynolds number flow remains unclear.

1.2 Literature review

1.2.1 Experimental and numerical study of bubble's motion and lift force in shear flow

Lift force was first analytically studied by Saffman (Saffman, 1965) by considering a sphere moving through a very viscous liquid in a uniform simple shear field with constant velocity. A correlation of lift force is proposed under the assumptions of $\mathrm{Re_b} \ll 1$as

$$F_L = \frac{81.2\mu V_r r_b^2 \omega^{1/2}}{\nu^{1/2}} \tag{1.3}$$

where μ and ν are fluid dynamic viscosity and kinematic viscosity. V_r is the relative velocity between two phase. r_b is the radius of the sphere and ω is the shear rate magnitude. However, this correlation has its limitation with its extremely low Reynolds number flow condition.

Ẑun (Ẑun, 1980) measured the lateral migration of bubble in vertical air-water flow. The bulk water Reynolds number range from approximately 5000 to 16000, and the equivalent diameter of the air bubble is between 0.64mm to 4.74mm. Based on experiment data, a lift force model was proposed as:

$$F_L = C_L \frac{4}{3} \pi \rho_f r_p^3 v_r \times (\nabla \times v_f) \tag{1.4}$$

where C_L is lift coefficient due to the net circulation of liquid around the ellipsoidal bubble and is around 0.3 according to their experiments. The format of this correlation is later used widely by the following researchers including Tomiyama (Akio Tomiyama et al., 2002) Auton (Auton, 1987) Legendre and Magnaudet (Legendre & Magnaudet, 1998) . Models proposed in their researches were developed by modifying the lift coefficient C_L depending on the bubble's size and different flow conditions.

Tomiyama (Akio Tomiyama et al., 2002) conducted experiments to study bubble transverse migration in water-glycerin solution. Experiment facilities used in their research are shown in Fig.1-1. The shear field was generated by rotating the belt immersed in the viscous fluid. The bubble was injected in the area between the moving belt and the wall. Experiment results show that, during the rising process, small bubbles (d_e <4.4mm) migrate to the direction of moving belt while large bubbles (d_e >4.4mm) migrate to the wall. The change of moving direction is caused by the sign change of the lift coefficient, which transits from positive to negative value with increasing diameter. The critical equivalent diameter for sign transition is 4.4 mm in their experimental conditions. The lift coefficient for small bubbles are well correlated by bubble Reynolds number while large bubbles are controlled by bubble Eötvo number. The critical bubble size diameter when the bubble changes its moving direction is close to the critical bubble diameter observed in upward air–water bubbly flow, which is between 5-6mm. Although the lift coefficient sign transition criterion is similar for high and low viscosity system, it does not guarantee that the lift coefficient correlation takes the similar formula in air-water system as proposed in high viscosity system. Results of Lee and Choi's experiment (Lee & Choi, 2014.) have shown that Tomiyama's model may not be applicable for the air-water system and needs to be evaluated by further experiments.

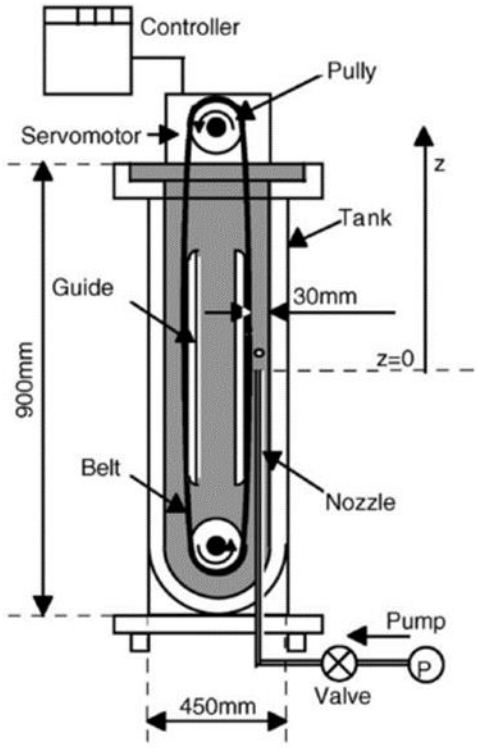

Figure 1-1: Schematic of Tomiyama's experiments apparatus (Akio Tomiyama et al., 2002)

Legendre and Magnaudet (Legendre & Magnaudet, 1998) studied the lift force on a spherical bubble by numerically solving the full Navier-Stokes equation. The bubble surface was assumed to be clean thus no shear is on the surface and there is no rotation of the bubble. Based on numerical results, a lift coefficient correlation for the spherical bubble was proposed in the range of $0.1<Re<500$. It was suggested that in low Reynolds number flow the lift force is dominated by the diffusion of vorticity on bubble surface. In high Reynolds number regime, the mechanism is associated with the presence of bubble causing asymmetrically distortion of the vorticity. Consequently, the lift coefficient decrease with Reynolds number and depends strongly on shear rate in low Reynolds number flow. However, from moderate to high Reynolds number regime, the lift coefficient is nearly independent of shear rate when $Sr \leq 0.2$.

Hibiki and Ishii (Hibiki & Ishii, 2007) intensively reviewed the existing works of lift force development in single particle system. Based on the work of Legendre and Magnaudet (Legendre & Magnaudet, 1998) , they introduced a factor in consideration of the deformation of bubble. The

critical diameter when the lift coefficient change its sign was found to be 5.70 mm. However, the application range of this model is relatively narrow with *Re* from 3.6 to 78.8.

W.Dijkhuizen et al. (Dijkhuizen, van Sint Annaland, & Kuipers, 2010) performed both numerical and experimental investigations of the lift force on single bubble in glycerin-water mixture. According to simulation result, it was interesting to notice that the shear rate magnitude has no influence on lift coefficient in intermediate Reynolds number flow. The lift coefficient partially agree with Tomiyama et al's model (Akio Tomiyama et al., 2002) in the region of 4< Eo <10.7. (Eo is Eötvös number and is defined as $Eo = \frac{\Delta \rho g d^2}{\sigma}$) Bubble with 6mm and 8mm equivalent diameter shows negative lift coefficient. A slanted wake was present behind the 8mm bubble and may be attributed to its negative lift coefficient. In addition, lift coefficient decreased from positive to negative value with decreasing aspect ratio. In high viscosity fluid, the transition of the lift coefficient value from positive to negative value occurs for nearly spherical bubble. For less viscous fluid, the critical aspect ratio when the lift coefficient change its sign is smaller and reaches hte limit at 0.45 for big bubbles. This coincides with Adoua et al's prediction (Adoua, Legendre, & Magnaudet, 2009) that the limit aspect ratio of the air bubble is close to 0.45. In terms of experiments, glycerin-water mixture with various viscosity was used. In contrast to simulation results, it was found that the shear rate magnitude has significant effect on lift coefficient under relatively low Reynolds number (1.0<*Re*<49) flow. Lift coefficient is positive for bubble with small Eo_H and changes its sign when Eo_H reaches critical value.

Adoua et al. (Adoua et al., 2009) numerically evaluated the lift force from moderate to high Reynolds number region in viscous shear flow. Results show that, in intermediate Reynolds number (*100<Re<1500*) and low shear flow field (*Sr*=0.02), the lift coefficient change its sign when bubble aspect ratio exceed critical value around 0.4-0.45. Streamwise vortices in the downstream of bubble was suggested to cause the lift force and the shear rate magnitude has no relation with the strength of lift force. A lift coefficient correlation was proposed as a function of aspect ratio and Reynolds number of the bubble.

Li et al.(Li, Song, Jiang, & Ishii, 2016, Li, Zhao, et al., 2016) investigated the single bubble motion in linear shear flow in water-air system for both small and relative large bubbles. The lift coefficient was found to be negative for small bubbles with different equivalent diameter from 2.24mm to 3.04mm under the shear rate of magnitude 0.5/s. It increases with increasing shear rate magnitude and decreases with increasing bubble size. The negative lift coefficient value of small bubbles disagrees with the results observed by Tomiyama et al, Dijkhuizen and Ishii and Hibiki (Akio Tomiyama et al., 2002, Dijkhuizen et al., 2010, Hibiki & Ishii, 2007). The lift coefficient value was found to be positive in their research. Water contamination, relative lower liquid viscosity, weaker shear rate magnitude and bubble generation method differences were suggested as potential reasons for this disagreement. While the disagreements exist for small bubbles, the lift coefficient has shown similarity for large bubbles ($10< d_e <20$mm) compared to the results obtained by other researchers mentioned above. The lift coefficient stays negative for all the bubbles in this range and decreases with increasing shear rate magnitude and bubble diameter.

Lee et al.(Lee & Choi, 2014) studied lift force with the L-shape channel as demonstrated in Fig. 1-2. Shear flow was generated by changing the flow direction with an L-shaped elbow and frictional vanes. Linear shear flow with shear rate magnitude equal to 3.98/s was obtained. Various sized bubbles ($0<Eo<35$) were investigated in high Reynold number region ($7470<Re<14740$) with bubble Reynolds number varying from 537 to 3300. It was found that large bubbles have negative lift force. While the trend of experimental data is well predicted by Tomiyama's model (Akio Tomiyama et al., 2002) , disparities exist in some cases. It suggested that the correlation developed with high viscosity fluid may not be applicable to the air-water system, which usually is associated with high Reynolds number flow and low viscosity.

The comparison of these experiments is made and presented in Table 1.1.

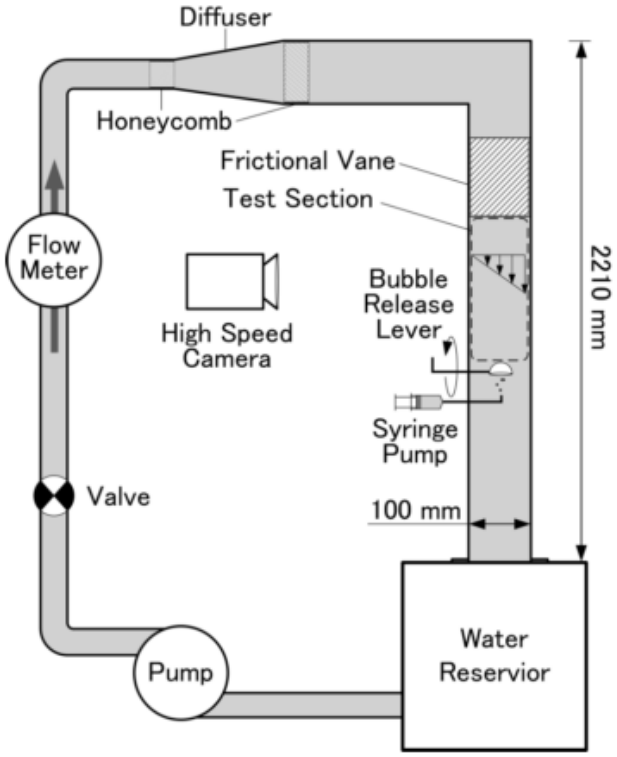

Figure 1-2: Schematic of experiment facilities in Lee et al's experiment (Lee & Choi, 2014.)

Table 1.1: Experimental study of lift force in linear shear flow

Investigator	Experiment conditions	Liquid type and flow condition	Bubble generation method	Remarks
Tomiyama et al. (2002)	$-5.5 \le \log_{10} M \le -2.8$, $1.39 \le Eo \le 5.74$, $0 \le S \le 8.3\ s^{-1}$, $2.8mm < de < 5.7mm$, $\mathrm{Re}_{bubble} < 100$	Co-current upward flow; Glycerol-water solution	Pitch –off	• $C_L = \begin{cases} Min(0.288\tanh(0.121\mathrm{Re}), f(Eo_H)) & Eo_H < 4 \\ f(Eo_H) = 0.00105 Eo_H^{\,3} - 0.0159 Eo_H^{\,2} - 0.0204 Eo_H + 0.474 & 4 \le Eo_H < 0.7 \end{cases}$. • Small bubbles have positive lift coefficient while large bubbles have negative lift coefficient.
W.Dijkhuizen et al. (2010)	$0.026 \le Sr \le 0.163$, $(1.0 < S < 4.0)$, $1.0 < \mathrm{Re} < 49$	Glycerol-water solution; Counter-current flow	Gentle push	• $C_L = MIN\left(\sqrt{\left(\frac{6J(\mathrm{Re},Sr)}{\pi^2\sqrt{\mathrm{Re}\,Sr}}\right)^2 + \left(\frac{1}{2}\frac{\mathrm{Re}+16}{\mathrm{Re}+29}\right)^2}, 0.5 - 0.11Eo_H + 0.002Eo_H^2\right)$ • Linear shear field has no consistent effect on drag coefficient. • C_L has strong dependency on the shear rate. It decrease with shear rate and Eo_h number.
S. Aoyama et al. (2017)	$1.9\times10^{-2} < \mathrm{Re} < 1.2\times10^{2}$, $2.2\times10^{-2} < Eo < 5.0$, $0 < Sr < 3.5$, $(0 < S < 7.4)$, $-6.6 \le \log M \le -3.2$	Glycerol-water solution; Co-current flow	Pitch-off	• A correlation of bubble aspect ratio proposed by Aoyama et al. has been verified in linear shear flow. • C_L decreases with increasing Re but increase with Sr. when Reynolds number is low. • C_L changes its sign when exceed critical bubble Reynolds number. • Critical bubble diameter ranges from 3 to 5.5 mm for $-13 \le \log M \le -3$.
Li et al. (2016)	$10mm < d_e < 20mm$, $S = 0.58s^{-1}, 0.62s^{-1}, 0.7s^{-1}$	Distilled water; Counter-current flow	Rotating hemi-spherical cup	• Small bubbles show negative lift coefficient and shear flow has no effect on bubble shape characteristic. • When bubble diameter exceed 15mm, C_L decreases with bubble diameter and shear rate magnitude have no effect.
Li et al. (2016)	$d_e = 2.24\ mm, 2.57\ mm, 2.70\ mm, 3.04\ mm$, $S = 0.4s^{-1}, 0.51s^{-1}, 0.57s^{-1}$, $440 < \mathrm{Re}_{bubble} < 600$	Distilled water; Counter-current flow	Gentle push	• C_L is negative in present experiment. It increases with shear rate magnitude and decreases with bubble diameter.
Lee et al. (2014)	$0 \le Eo_H \le 35$, $7470 \le \mathrm{Re}_{channel} \le 14740$, $537 \le \mathrm{Re}_{bubble} \le 3300$, $S = 3.98s^{-1}$	Unknown water quality; Counter-current flow	Rotating hemi-spherical cup	• $C_L = -\frac{5}{8}\tanh\left(\frac{Eo-5.5}{6}\right) \quad 0.6 < Eo < 32$ • C_l keeps negative and stay as constant value for the large bubble. • Bubbles with spiral motion and zigzag motion shown scattered lift coefficient value.

1.2.2 Shear flow generation

Because lift force is closely related to the shear flow field, it is important to generate stable linear shear flow. In review of the literatures, various methods have been proposed to generate shear flow for gas and liquid flow.

Chen et al. (Chen, Milos, & Kotansky, 1966) studied the application of honeycomb in a wind tunnel and used it to generate a layer of linear shear flow field bounded by two layers of uniform flow; however, this method has not been applied and validated in liquid flow.

Owen and Zienkiewicz (Owen & Zienkiewicz, 1957) generated uniform shear flow in a wind tunnel by inserting non-uniform parallel spacing rods in the flow field and observed the linear field. It might be able to generate linear shear flow by strategically arranging the rods. However, no detailed information was given on the configuration of rods.

Constant and non-constant properties curved screen had been used by Elder, Turner, Castro et al.(Elder, 1959, Turner, 1969, Castro, 1976) to generate shear flow and had been optimized for application in water flow experiments.

Tomiyama et al. (Akio Tomiyama et al., 2002) generated the linear shear flow by immersing a rotating belt in glycerol-water solution. This method can generate high shear rate up to 8/s on a small scale. However, it requires high viscosity fluid and the small scale limits bubble size. Additionally, it may introduce wall effect to the behavior of bubble motion.

Lee et al. (Lee & Choi, 2014) used a L-shape channel and friction vanes to generate high shear rate (ω=3.98/s) within a rectangular channel. It provides a promising method to generate high shear rate magnitude in low viscosity fluid. However, no detailed information was given on the distribution of the friction vanes.

W.Dunn and S.Tavoularis (Dunn & Tavoularis, 2007) summarized the methods stated above and pointed out that a single curved screen is the most appealing method to generate uniform shear flow without introducing much turbulence in the downstream of the flow field. Theoretical correlations were given to determine the curved shape based on the expected shear rate. A prototype curved screen was built and the linear shear field was observed in their experiment. In addition, Li et al. (Li, Zhao, et al., 2016) applied the curved screen method in their experiment and good linear shear flow was obtained.

In this experiment, the curved screen method is selected to obtain the linear shear field, in consideration of the available knowledge and manufacturing facilities.

1.3 Motivation

In BWR and accident scenarios of PWR, two-phase flow in the reactor core channel is expected to occur. The void fraction distribution will significantly affect the heat transfer process within the reactor core in this case. Thus, it is of importance to understand how void fraction distribution occurs in both axial and radial directions. The lift force was considered to be a major force governin the void distribution in the radial direction; however, there lacks a solid model to predict its force.

According to literature review, only few experiments are performed to study lift force, and most experiments were performed using high viscosity fluid. Also, the flows were mainly in relative low Reynolds number. The lift force in low viscous flow is not clear, and shows some disparities with those experiments conducted with high viscous fluid. As Li et al.(Li, Zhao, et al., 2016) mentioned, small bubbles have negative lift coefficient under the low shear rate magnitude flow while the lift coefficient for small bubble with high viscous fluid usually has positive value. The reason causing this disagreement is not clear yet.

.

In summary, more experimental data in air-water two-phase flow are required in order to evaluate existing models and for further model development.

1.4 Objective

This study intends to generate linear shear flow for the study of lift force in two-phase flow system. The curved screen method for shear flow generation is evaluated.

In addition, characteristics of bubble motion including terminal velocity, bubble aspect ratio, oscillation amplitude and lift force will be investigated under different flow conditions. The results obtained in this study will be compared with existing models for evaluation and also provide valuable data for further lift force study and bubble dynamics study.

1.5 Thesis outline

A detailed introduction of experiment facilities and all the instruments used in this experiment will be discussed in Chapter 2. Chapter 3 will talk about the shear rate magnitude measurement and analysis procedure of bubble motion. Results and discussions are presented in chapter 4. Lastly, Chapter 5 will summarize all the work and discoveries in this study and give a prospect of future research.

CHAPTER 2. EXPERIMENTAL SETUP

2.1 Instrumentation

This section gives comprehensive introduction of instruments used in this research and the principles on how these instruments works.

2.1.1 Electromagnetic flowmeter

An electromagnetic flowmeter (Honeywell MagneW 3000) is used in the loop to measure the average flows velocity in the test section. A magnetic field is generated inside the metering tube. When water flows through the flow meter, it creates a potential difference proportional to the flow velocity. Due to this mechanism, the fluid must be conductive, thus conductive solution must be added to the pure water to increase its conductivity. Output signal of the flowmeter is a 4-20 mA current. The current signal is converted to voltage signal by resistor (250 ± 1 ohm). The voltage signal is converted to flow rate by the computer. According to the manufacturer, uncertainty of this flowmeter is $\pm$ 1.1 %.

2.1.2 Laser Doppler Velocimetry (LDV)

LDV is a state-of-the-art non-intrusive measurement technique for transparent or semi-transparent fluid flows. Integrated with laser and modern computer technology, this facility is being used widely for flow dynamics analysis. The LDV system used in this study (DANTEC DYNAMICS BSA.F30) is manufactured by DANTEC company. Fig.2-1 shows the principles of how LDV works.

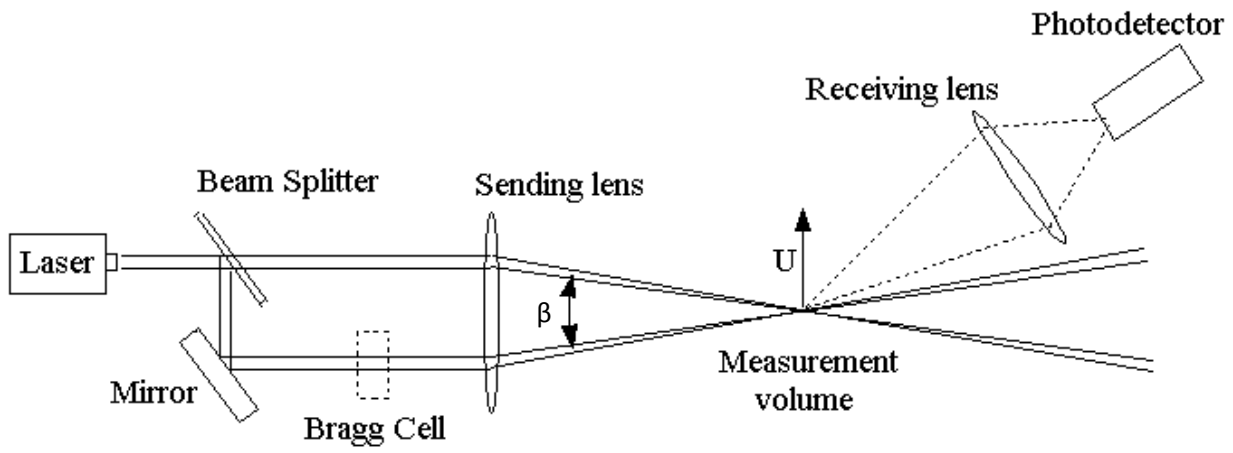

Figure 2-1: Schematic of LDV measurement

A beam is generated by the laser machine and split into two beams with same frequency and phase. One beam's phase is changed by passing a Bragg cell. Two beams are refracted by the lens and cross at a focal point, where the measurement process occurs. Due to the Doppler interference, these two beams generate a fringe pattern with light and dark strips in the measurement volume as shown in Fig. 2-2. Seeding particles follow the flow in fluid and pass through the fringes. When seeding particles pass through the light strips, light is reflected into the photodetector. The light signal is converted to electrical signal and processed by the computer. The fringe distance d_{fringe} can be calculated from the wavelength λ of the laser light and the angle between two beams β as follows:

$$d_{fringe} = \frac{\lambda}{2\sin(\beta/2)} \tag{2.1}$$

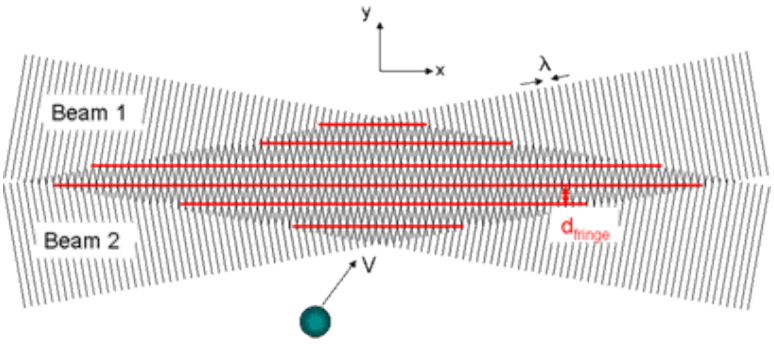

Figure 2-2: Fringe pattern in LDV measurement volume

As particles reflect the flow velocity of the fluid, the flow velocity is obtained as:

$$v = \frac{\mathrm{d}_{\mathrm{fringe}}}{\Delta t} \tag{2.2}$$

where Δt is the passing time of particles and can be obtained through the scattering light signal.

In order to best track the flow behavior, different particles need to be selected for different fluid flow. The sedimentation velocity of seeding particles in fluid and response time of a particle in fluid is given as (Raffel et al., 2018)

$$V_s = \frac{\Delta\rho d_p^2 g}{18\mu} \tag{2.3}$$

$$\tau_p = \frac{d_p^2 \Delta p}{18\mu} \tag{2.4}$$

The particles used in this study are hollow glass spheres with 10μm diameter, and their density is 1.1g/cm^3. Corresponding sedimentation velocity and response time are 6.12×10^{-6} m/s and 6.24×10^{-7} s respectively. The error is negligible compared to the water velocity magnitude in this experiments.

2.1.3 High speed camera

After releasing a single bubble into the flow field, the bubble rises up in view section, and the high speed camera is used to capture the motion of the bubble. The high speed camera used in this experiment is Photron Fastcam SA3. Frame rate is set to 500fps and image size of 1024×1024 pixel is chosen after balancing the size of file and image quality. The lens used for this camera is Vivitar 19mm-24mm wide angle lens, which provides wide angle view.

The raw images captured by this high speed camera are later processed by MATLAB to obtain the properties of bubble and its motion characteristics such as the aspect ratio, bubble equivalent diameter, terminal velocity etc.

2.2 Experimental facility

The experiment facility is illustrated in Fig. 2-3. Water is supplied by a centrifugal pump and flow from top to bottom of the test section. The flow cross section is 203.2mm in length and 76.2mm

in width. Detailed dimension of the facilities is illustrated as below in Fig. 2-4. Plastic honeycomb with thickness around 70mm is installed in the top part of the channel, acting as a flow collimator. Velocity is uniformed by the honeycomb first and then the flow is converted to linear shear flow in the downstream after flowing through the curved screen. The mechanism of this conversion will be discussed in Chapter 3. The flow rate is adjusted by controlling pump frequency and valves in the loop. Flow rate is regulated and monitored by the electromagnetic flow meter. Since water quality has significant influence on the bubble motion, it is of great importance to use pure water without any particles or contamination. The deionized water used in this experiment is obtained from tap water filtered by 4 tanks provided by Kokomo Inc. The water quality is determined by referring to its conductivity level. Water conductivity of the filter tanks outlet is kept in the range of 0-5 $\mu S / cm$ during the experiments and the temperature of the water is kept at 24°C.

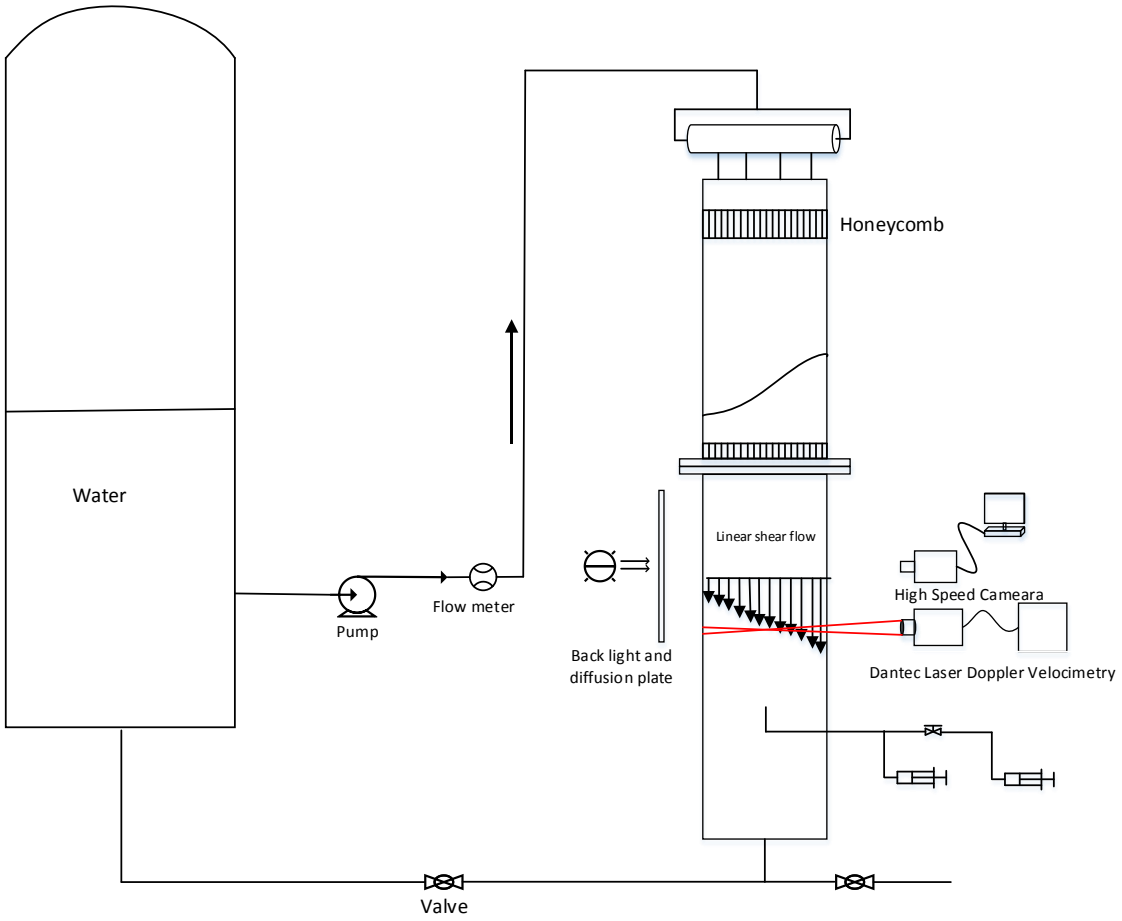

Figure 2-3: Schematic of experiment facility

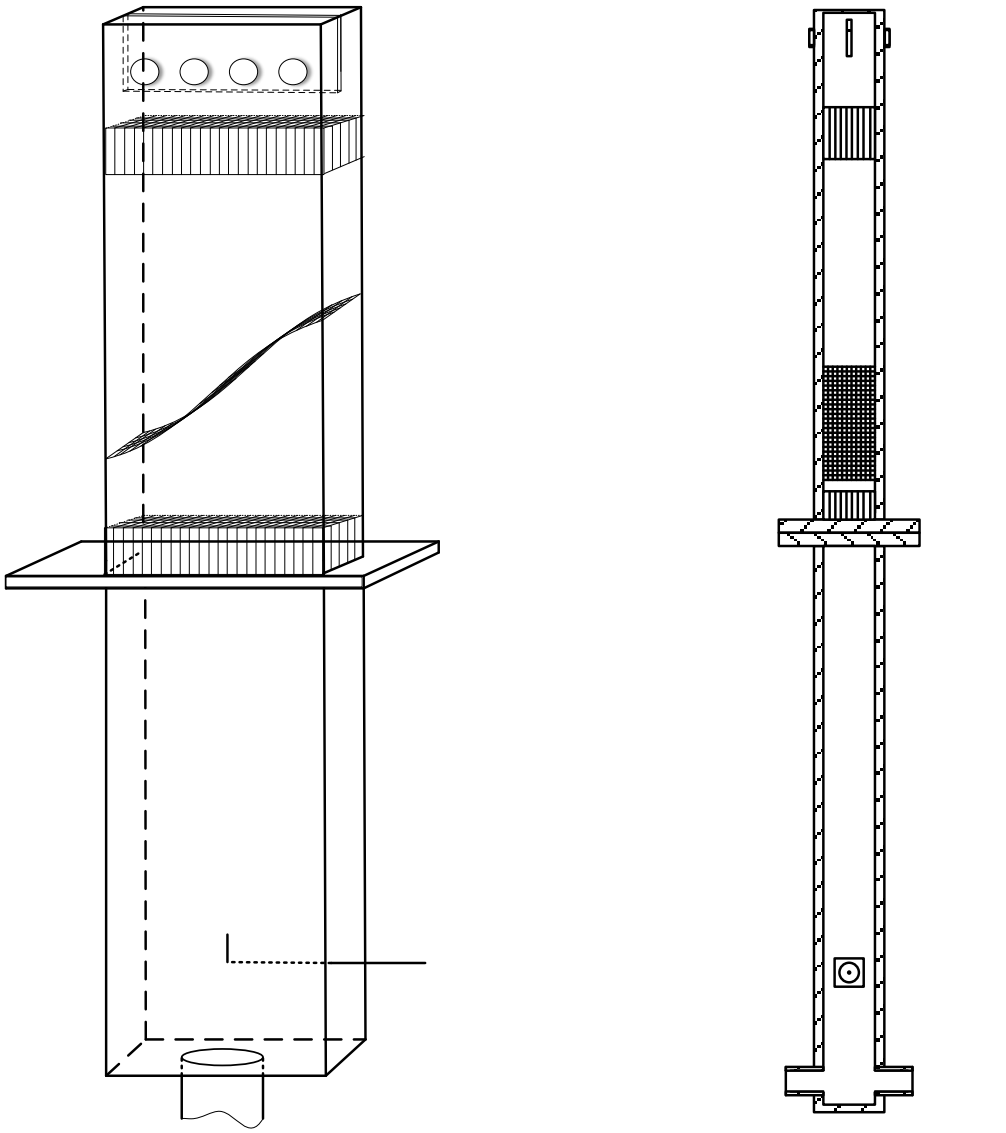

(a) 3D view of channel (b) Side view of channel

Figure 2-4: Scheme diagram of experimental facility (units: mm)

Figure 2-4 continued

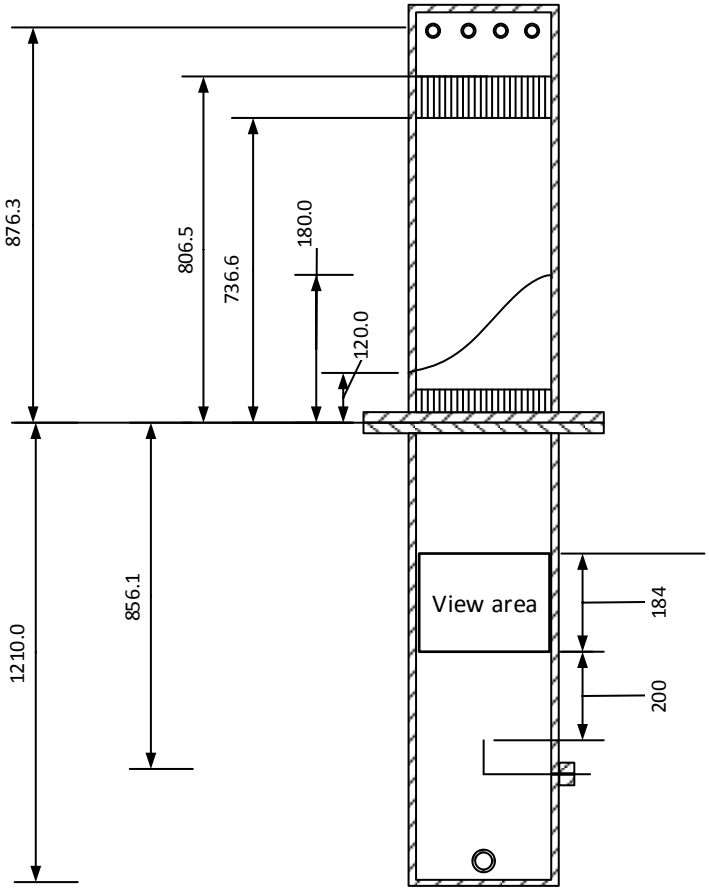

(c) Dimension of flow channel

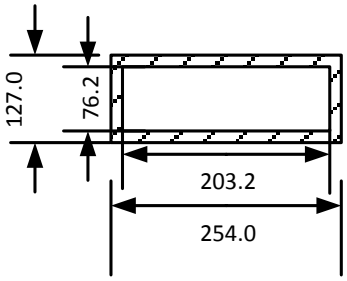

(d) Dimension of flow cross section

2.2.1 Linear shear flow field generation

As discussed previously in chapter 1.2.2, several methods were proposed to generate linear shear flow. In the present experiment, the curved screen is selected. The wire diameter and wire distance of the screen used in this experiment are 0.23mm and 0.51mm, respectively. Solidity of the screen is 0.7 and its corresponding Reynolds number is about 33.

Fig. 2-5 shows the schematic of the linear field generation. Flow velocity was uniformed by the honeycomb in the upstream of curved screen. After flowing through the screen, the uniform flow is converted to linear shear flow. Fig. 2-6 shows the shape of curved screen used in this experiment with designed shear rate magnitude of 0.9s at average flow velocity -0.15m/s. The shape of the curved screen can be determined using equation 2.3 and equation 2.4.(Dunn & Tavoularis, 2007)

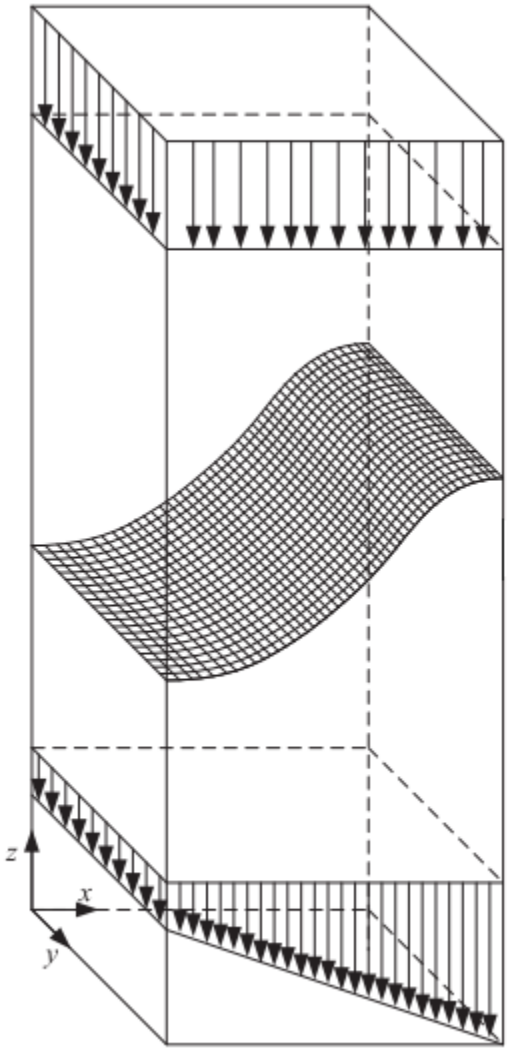

Figure 2-5: Schematic of shear flow generation

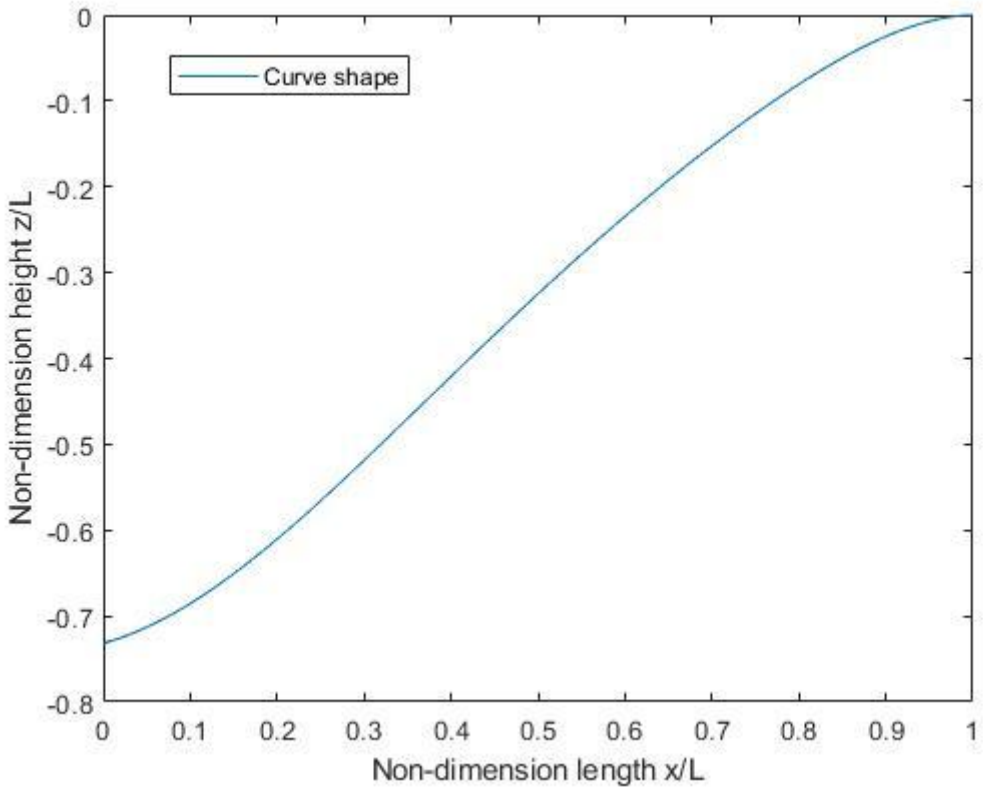

Figure 2-6: Dimensionless curve shape

$$f(\frac{x}{L}) = -0.738(\frac{x}{L})^6 + 2.812(\frac{x}{L})^5 - 3.839(\frac{x}{L})^4 + 2.687(\frac{x}{L})^3 - 1.224(\frac{x}{L})^2 - 0.0054(\frac{x}{L}) \quad (2.5)$$

$$\frac{z}{L} = \frac{(2+K-B)\beta}{KB} f(\frac{x}{L}) \quad (2.6)$$

2.2.2 Bubble generation

A single bubble is investigated at a time in order to eliminate the effect induced by bubble interaction such as coalescence and disintegration. In addition, the leading bubble will create a wake area behind which has significant influence on the following bubbles. Thus the time interval between each bubble injection was kept long enough for the flow field to reach stable status.

As mentioned by Tomiyama et al. (Akio Tomiyama et al., 2002) and Wu et al. (Wu & Gharib, 2002) , the bubble terminal velocity and aspect ratio depend on its initial deformation at the releasing point. The initial deformation is affected by the size of the capillary tube and bubble

generation methods. Capillary tubes with large diameter tend to generate small deformation bubble while small tubes tend to generate large deformation bubble.

According to literature review, three methods were typically used to generate bubble, which are the pitch-off method, gentle push method, and hemi-sphere rotating method. In terms of the pitch-off method, air is injected into the flow field directly through the capillary tube by slowly pumping air into the tube. When the bubble buoyance force is larger than the surface tension force and drag force combined in the flow field, the bubble will detach naturally from the tube tip. For the pitch-off method, the bubble size is not able to be adjusted and is determined only by needle size. The gentle push method uses two syringes to generate the bubbles. The first syringe is filled with air, and the second syringe is filled with water. A specific amount of air is injected into the tube by the air syringe and then the water syringe is used to gently push the bubble out. By adjusting air volume in the tube, this method can generate bubbles with wide range of diameters. However, both methods cannot produce large diameter bubbles due to the limitation of the tube size. Larger diameter bubble is generated and released by rotating a hemisphere spoon in the flow. As shown in Fig.2-7, a specific volume of air is injected through the tube and accumulated in the spoon. After reaching a specific volume, the bubble is released by rotating the spoon. By controlling the amount of air accumulated in the spoon, this method can generate various size bubbles.

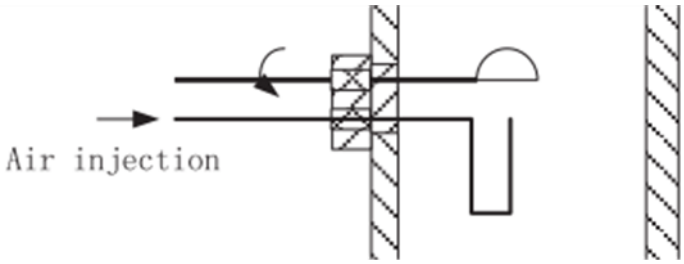

Figure 2-7: Schematic of rotating spoon method to generate bubble

In this experiment, the gentle push method fails due to the many bends and tube connectors obstructing the path of small bubbles to reach the needle tip. Thus the pitch-off method is applied to generate small size bubbles. To generate different size bubbles, needles with various diameter were applied. Small amount of air (larger than one bubble volume) is injected into the capillary tube first by air pump, and then the water syringe was used to push the air out at a rate of 0.75ml/min, which is slow enough for the bubble to detach from the needle tip naturally. This

method can reduce the volume expansion or compression induced by the high pressure inside the tube.

CHAPTER 3. ANALYSIS PROCEDURE

3.1 Linear shear flow measurement

As the curved screen method is selected to generate shear field, the shear rate magnitude is determined by various factors including upstream flow velocity, curve shape, screen mesh size, wire size etc. Once the curved screen is manufactured, all other factors are determined by the physical properties of the screen except for upstream flow velocity. Thus shear rate is controlled by upstream water flow velocity. High velocity would generate higher shear rate magnitude and vice versa.

The shear rate is obtained by linearly fitting the velocity in the downstream of the curved screen. The velocity of flow is measured by the LDV system, which requires seeding particles. Before running the experiment, the seeding particles and conductive chemicals Morpholine and Ammonium are added to the water. This fluid mixture is circulated in the loop for several minutes in order to mix uniformly the seeding particles and conductive chemical with water. Water conductivity is adjusted to be 20-30 $\mu S / cm$ as required by the electrical flow meter. The downward flow velocity of water cannot be too large as small bubbles would be flushed downward due to drag force acting on the bubble. Two average fluid velocities -0.1m/s and -0.15m/ are selected in order to make all the bubbles with different diameters rise up in the flow field.

Vertical velocity measurement is performed at two vertical positions (Z=200mm, and Z=400mm) and three parallel planes (y=0.4W, y=0.5W and y=0.6W) as shown in Fig.3-1. The needle tip point is marked as Z=0mm.

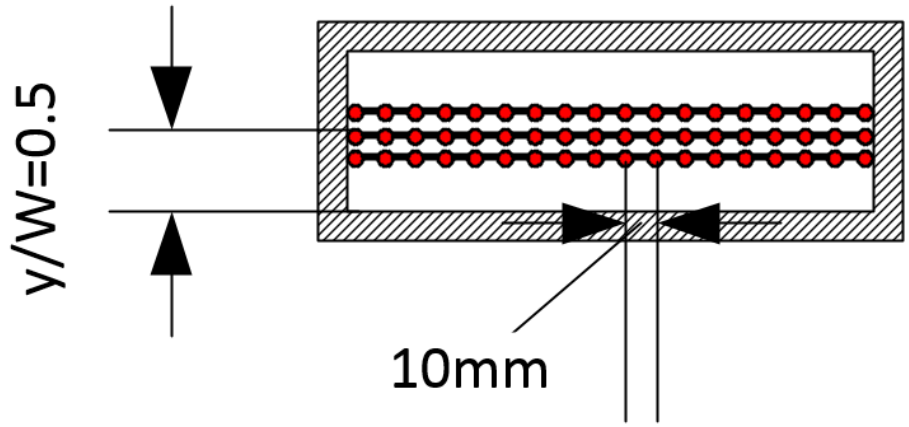

Figure 3-1: Velocity measurement points

Fig. 3-2 below shows the velocity profile in the bottom and top plane in the view section. For each point, 300 velocity samples are measure to determine the velocity. After 300 samples, there is no major change of the measuring velocity and the minor change is within 5%. The validation rate of each measurement point is over 98%. The velocity profile in the close wall region does not show good linearity due to high viscosity and wall effect. Thus only the points between $0.2<x/L<0.8$ are selected to fit the shear rate magnitude linearly and considered to be the linear field.

Lift coefficient is calculated based on the lateral migration velocity of the single bubble and relative velocity of bubble and water. It was assumed that lateral migration of the bubble is the results of the lift force exclusively. Small velocity component in the lateral direction would have significantly influence on the bubble's lateral motion. The effect of the lateral velocity component within the flow velocity needs to be eliminated. In order to check this lateral component velocity, horizontal velocity measurement is also performed in the center plane at Z=200mm and Z=400mm.

As shown in Fig. 3-2, both positions in Z=200mm and Z=400mm have good linearity. The shear rate magnitudes in position Z=200mm are -0.630, -0.910 and Z=400mm are -0.650, -0.912, respectively. The corresponding average flow rates are -0.1m/s and -0.15m/s. Shear rate in upstream is slightly larger than that in downstream position, and this may be attributed to turbulence diffusion. Hence, flow field tends to become more uniform with increasing distance to the curved screen. The difference between the shear rates of the top and bottom planes is within

5%, thus the flow field between this these two planes can be regarded as linear shear flow. The mean values of the shear are obtained by taking the average value of shear rate in top and bottom planes, which are 0.640 and 0.911. Although good linearity is shown in the flow field, large lateral velocity is found in the plane as shown in Fig.3-2 (e). The maximum absolute value of the lateral velocity reaches 10mm/s when the average downward flow velocity increases to 0.15m/s.

In Li et al.'s experiment (Li, Zhao, et al., 2016), bubbles with small and large diameter migrate to one direction and there is no transition for lift coefficient from positive to negative value as other research indicated. Water velocity changes its direction from straight downward to normal to the screen when it flows through the screen. The lateral velocity existed in the flow field may cause this disagreement, and the lateral velocity component is introduced by the curved screen.

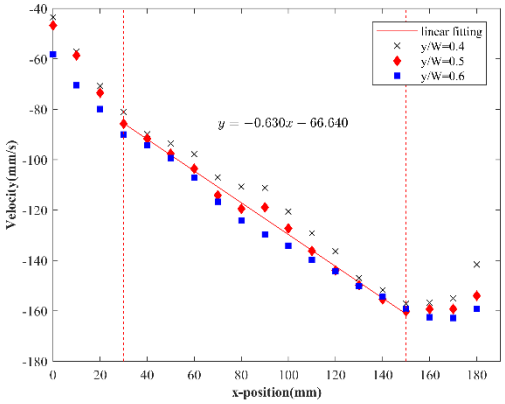

(a) $z = 200mm$, $j_f = -0.1m/s$

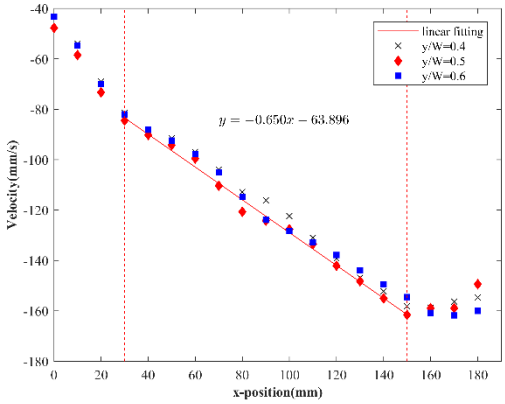

(b) $z = 400mm$, $j_f = -0.1m/s$

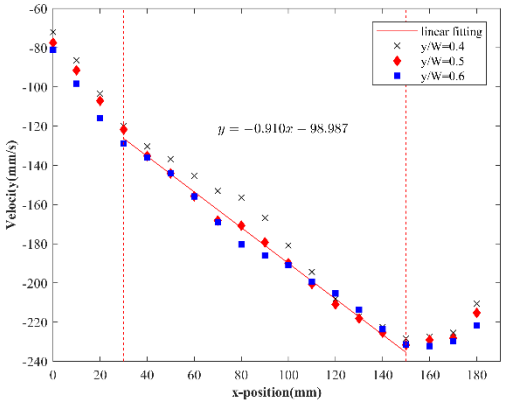

(c) $z = 200mm$, $j_f = -0.15m/s$

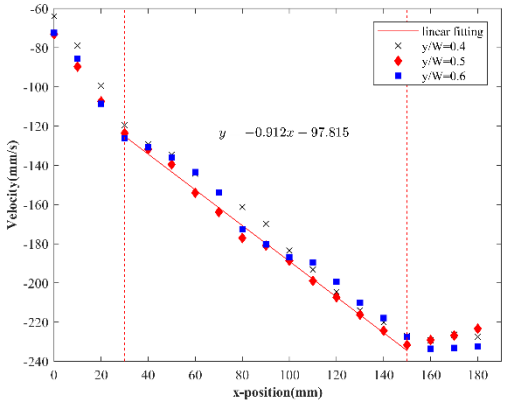

(d) $z = 400mm$, $j_f = -0.15m/s$

Figure 3-2: Shear flow profile without flow collimator in the downstream

Figure 3-2 continued

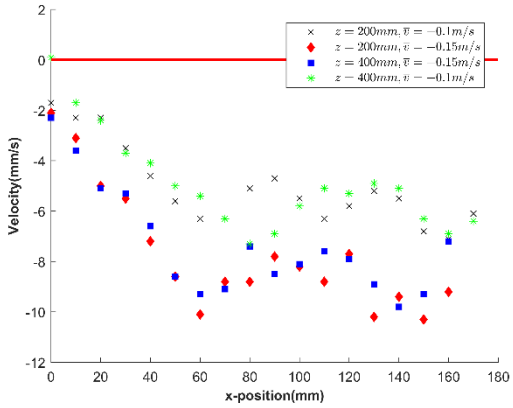

(e) Horizontal velocity

To eliminate lateral velocity in the downstream test section, a honey comb with thickness of 10cm is installed in the downstream of the screen as a flow collimator. Flow profile is measured again and the new velocity profile is plotted in Fig.3-3. Under the same flow velocities -0.1m/s and -0.15m/s, shear rate magnitudes in position *Z*=200mm decreased from 0.630/s and 0.910/s to 0.306/s and 0.451/s, respectively. In position *Z*=400mm, the shear rate magnitudes decrease from 0.650/s and 0.912/s to 0.336/s and 0.476/s, respectively. The average shear rates are 0.321/s and 0.464/s by taking the average of top and bottom plane shear rates. Decrease of shear rate magnitude under the same flow rate is attributed to friction of the honeycomb causing the flow to become more uniformed. Also, the top plane has lager shear rate magnitude compare to the bottom plane due to turbulence diffusion. While the shear rate is reduced to about half of the previous value, the lateral velocity significantly reduced to around 0 mm/s under the same flow rate as shown in Fig3-3 (e).

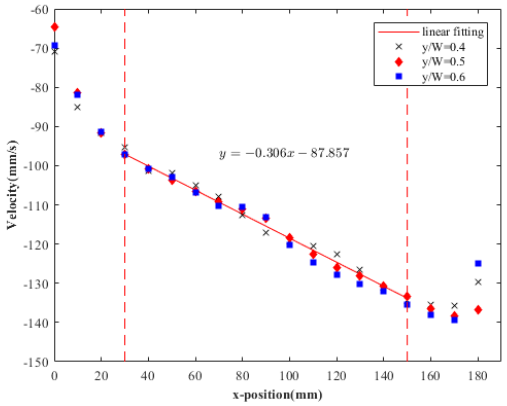

(a) $z = 200mm,\ j_f = -0.1m/s$

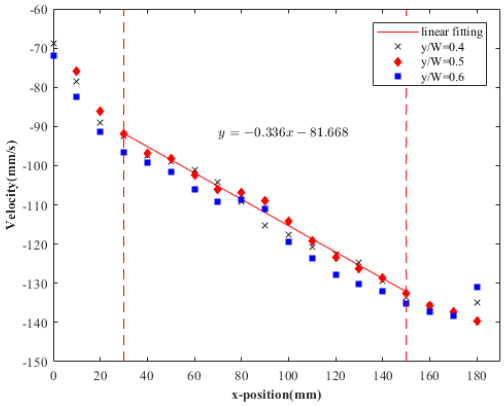

(b) $z = 400mm,\ j_f = -0.1m/s$

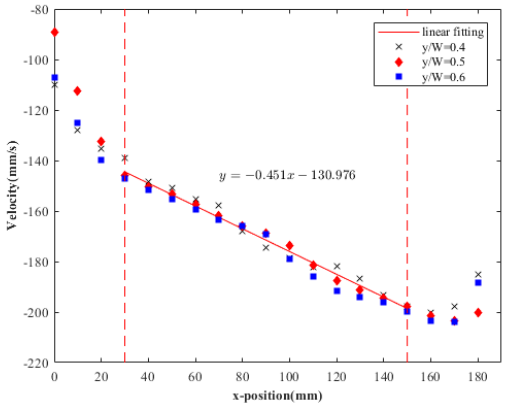

(c) $z = 200mm,\ j_f = -0.15m/s$

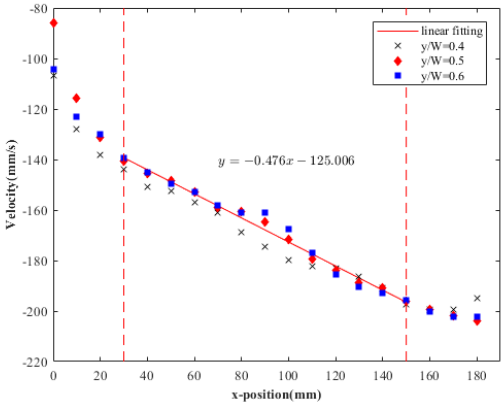

(d) $z = 400mm,\ j_f = -0.15m/s$

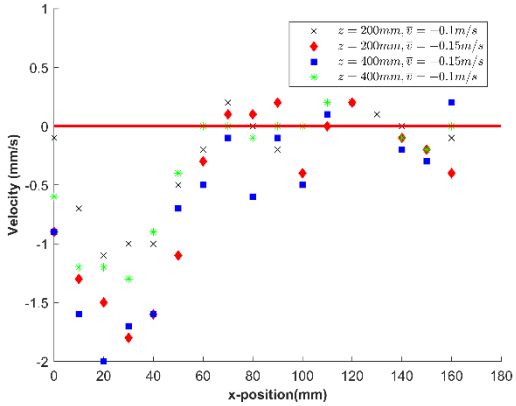

(e) Horizontal velocity in 4 flow conditions

Figure 3-3: Shear flow profile with flow collimator in the downstream

Table 3.1 gives comparison of the shear rate magnitude before and after installing the honeycomb.

Table 3.1: Shear rate magnitude

Flow Velocity / Positions	-0.1m/s		-0.15m/s	
	Before installing the honeycomb	After installing the honeycomb	Before installing the honeycomb	After installing the honeycomb
Z=200mm	0.630/s	0.306/s	0.910/s	0.451/s
Z=400mm	0.650/s	0.336/s	0.912/s	0.476/s
Average	0.640/s	0.321/s	0.911/s	0.464/s

3.2 Bubble characteristic analysis

After the LDV measurement is done, water is drained and the test section is flushed for many times with pure water to eliminate the seeding particles and their potential influence. Then the loop is filled with water with conductivity adjusted to 20-30 $\mu Sv/cm$. The water is circulated in the loop for several minutes.

When the flow reaches a stable state, a single bubble is injected into the channel center and its trajectory is captured by high speed camera. Raw captured images are then processed using MATLAB image processing package. The following sections give information on how each image is processed. The analysis of bubble rising characteristics consists of the following subjects (1) bubble horizontal and vertical diameter, (2) bubble aspect ratio, (3) bubble rising velocity, (4) bubble oscillation amplitude, (5) bubble lateral migration velocity.

Due to instability of bubble motion in the water, some bubbles migrate close to the wall region and out of the linearity shear field. In order to avoid wall effect on the bubble's motion, a side-view web-camera is amounted to monitor the trajectory of rising bubbles. Only bubbles rising in the range $0.4 < y/W < 0.6$ are captured for processing.

3.2.1 High speed camera setup and calibration

It was confirmed that the bubble reaches its terminal velocity after rising 170mm in the water (A. Tomiyama et al., 2002, Celata, Cumo, Annibale, & Di, 2006). The bottom edge of the view

window is 200mm above the release point, leaving enough space for the bubble to reach terminal velocity and rise in quasi-steady state.

The frame rate of the camera is set to be 500 to reduce data size without degrade the quality of the image. In order to determine the bubble's boundary more precisely, a diffusion plate with back light is set up to illuminate the measuring area and help improve the contrast between the bubble boundary and surrounding liquid.

In order to know the scale ratio of pixel to real size, a rigid object is immersed in the water in the middle plane of measuring area (y=0.5W) and a photo of it is taken by the high speed camera. The corresponding pixels values of this rigid object is easy to measure and the ratio of pixel value to real size is obtained. In the current camera setup configuration, the rigid object is 100mm in length and the corresponding pixel value is 555 ± 10 pixels. Thus one pixel equals to 0.18mm in real size, and the maximum error obtained is 1.80%.

The high speed camera is mounted on a tripod. It is necessary to mention that even a small angle of deviation from the vertical direction will introduce large error to the bubble lateral migration distance. To ensure accurate alignment, a sprit level is placed on top of the camera and the tilt angle was kept within $0° \pm 0.2°$. Assuming the bubble rises about 140mm in the view area, the maximum lateral displacement caused by camera tilting is

$$140 \times (\pm \tan(0.2^{\circ})) = \pm 0.49 mm \quad (3.1).$$

3.2.2 Bubble edge detection

The raw images captured by the high speed camera are processed by MATLAB using its image processing code Digital Image Processing (DIP) Package. This section gives the routines on how to analyze bubble motion characteristic.

Fig 3-4 shows the routine of the bubble image processing. First, a reference picture without the bubble is chosen as the background image and all the images with bubbles subtract this background image, after which only the bubble information is left. The contrast of the bubble in each image is

enhanced. Then each image is converted into a binary image for dilation, erosion and hole filling processing. The bubble characteristics such as the center position, boundary position, projected area and aspect ratio are obtained after these steps. By repeatedly analyzing the bubble in each frame, the bubble moving velocity can be calculated and the shape evolution is obtained.

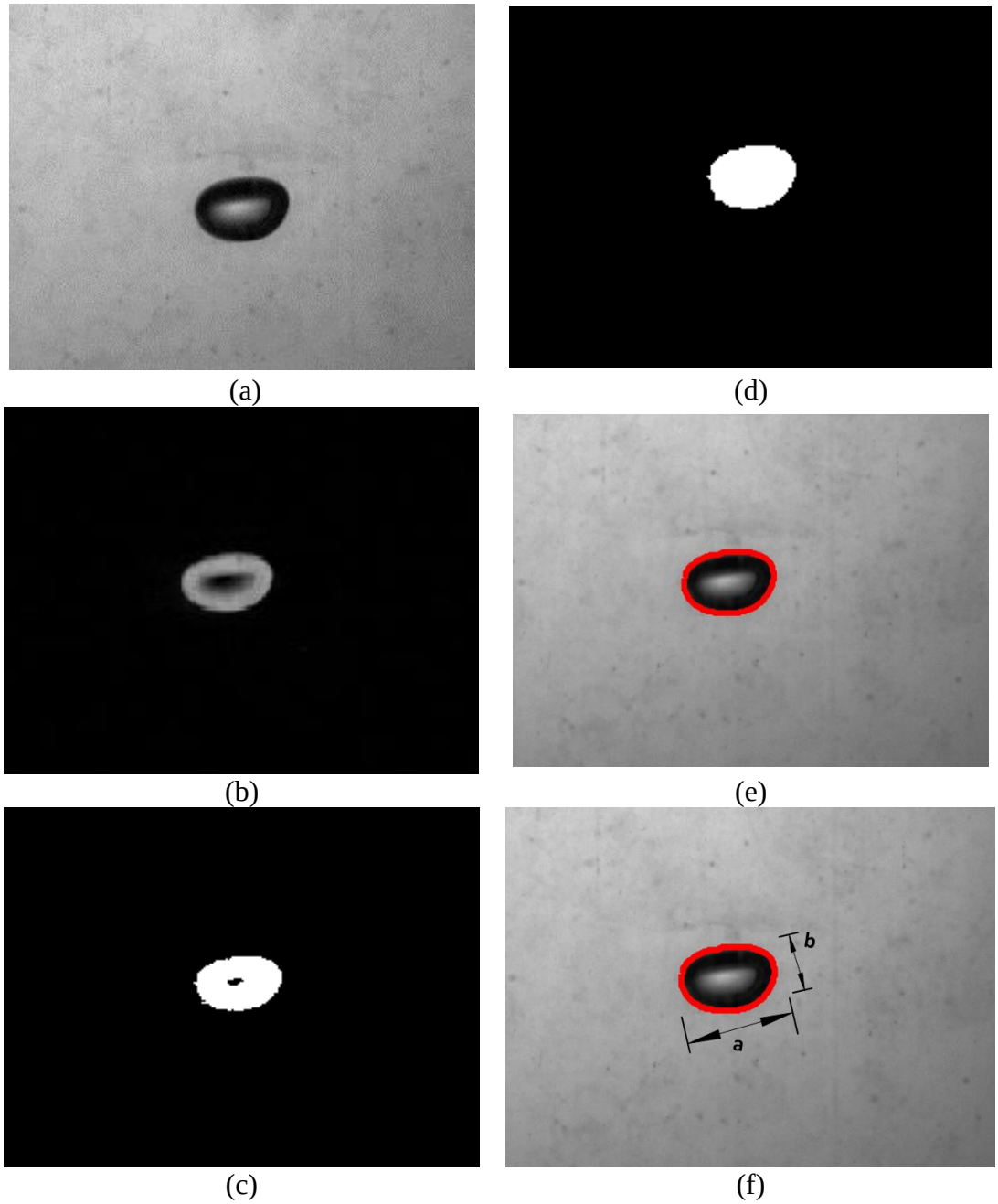

Figure 3-4: Image processing routine

(a) Raw captured bubble image, (b) Background subtraction, (c) Contrast adjustment, (d) Hole filling, (e) Bubble edge detection, (f) Horizontal diameter and vertical diameter of bubble

Fig 3-5 and Fig 3-6 show a typical bubble trajectory and its evolution in coordinate. Solid black line denotes bubble volume center position in each frame, and red contour denotes bubble contour per 0.05s.

Figure 3-5: Typical bubble motion trajectory

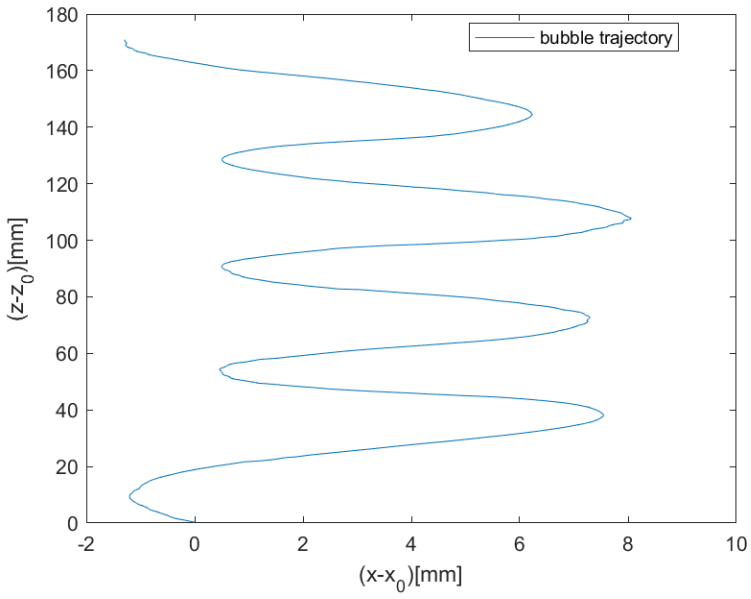

Figure 3-6: Bubble trajectory in coordinate

Due to the blurred bubble edge, the algorithm would detect the edge of the bubble with uncertainty around one pixel. The uncertainty of this measurement decreases with growing size of the bubble. It is within 10% when the bubble equivalent diameter is larger than 3mm and declines to 2% when bubble size reaches 20mm. Fig. 3-7 gives the uncertainly level versus the bubble diameter in this experiment.

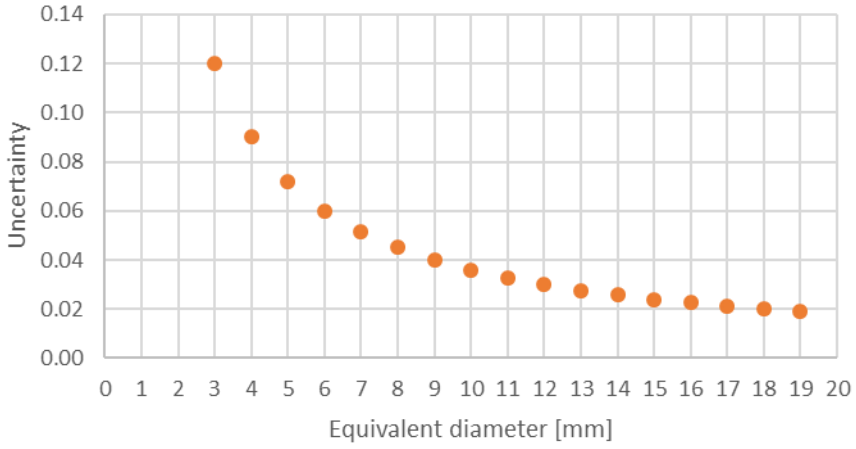

Figure 3-7: Measurement uncertainty decrease with bubble size

3.2.3 Bubble size

Equivalent diameter is a major characteristic describing the size of a single bubble. There are two approaches to calculate it; one method uses the projected area of bubble to determine its value. The area *S* can be easily obtained by referring to the amount of pixels occupied by the bubble in each image. As a result, equivalent diameter is given as:

$$d_e = 2\sqrt{S/\pi} \tag{3.2}$$

This approach works well when bubble diameter is small and close to spherical shape. However, with increasing bubble diameter, the bubble shape changes to oblate spheroid. In addition, the bubble volume expands more or less as a function of the vertical position since the hydrostatic pressure decreases with height. Diameter calculated from the projected area would introduce large error. Therefore, a better approach is to calculate the equivalent diameter from the major and minor axis length of the bubble (Dijkhuizen et al., 2010),which is

$$d_e = \sqrt[3]{a^2 b} \tag{3.3}$$

where a and b are the major axis and minor axis, respectively, as shown in Fig.3-4 (f).

The equivalent diameter of each bubble is obtained by averaging the diameters in all frames.

$$d_e = \frac{\sum_{i=1}^{n} d_{ei}}{n} \tag{3.4}$$

3.2.4 Aspect ratio

The aspect ratio is a parameter reflecting the shape deformation of a bubble; it is defined as:

$$E = \frac{b}{a} \tag{3.5}$$

For bubbles with irregular shape, the major and minor axis lengths are obtained by assuming the bubble shape as a symmetric ellipsoid with the same projected area. As the bubble rises up with zigzag or helical motion, the aspect ratio continually fluctuates around the average value.

3.2.5 Oscillation amplitude

It was observed by many researchers (Peters & Els, 2012, Maldonado, Quinn, Gomez, & Finch, 2013, Celata et al., 2006) that the bubble usually rises up in liquid in zigzag or helical motion. However, the experimental investigation on bubble oscillation amplitude is rare. In multiple bubble systems, interactions between the bubbles would be important, and oscillation will influence the interactions. Since only one camera is available for the experiment, it is difficult to distinguish the zigzag and helical motions directly. Thus, the 3D motion would be analyzed by its projected trajectories in the 2D plane.

Fig. 3-8 shows a typical bubble lateral moving distance versus time. The original curve is smoothed out in order to find its peak and valley points. The oscillation amplitude for each bubble is then obtained as follows:

$$O_s = \frac{L_o}{m} \tag{3.6}$$

where O_s is average oscillation amplitude. L_o is total lateral moving distance and m is total oscillation times.

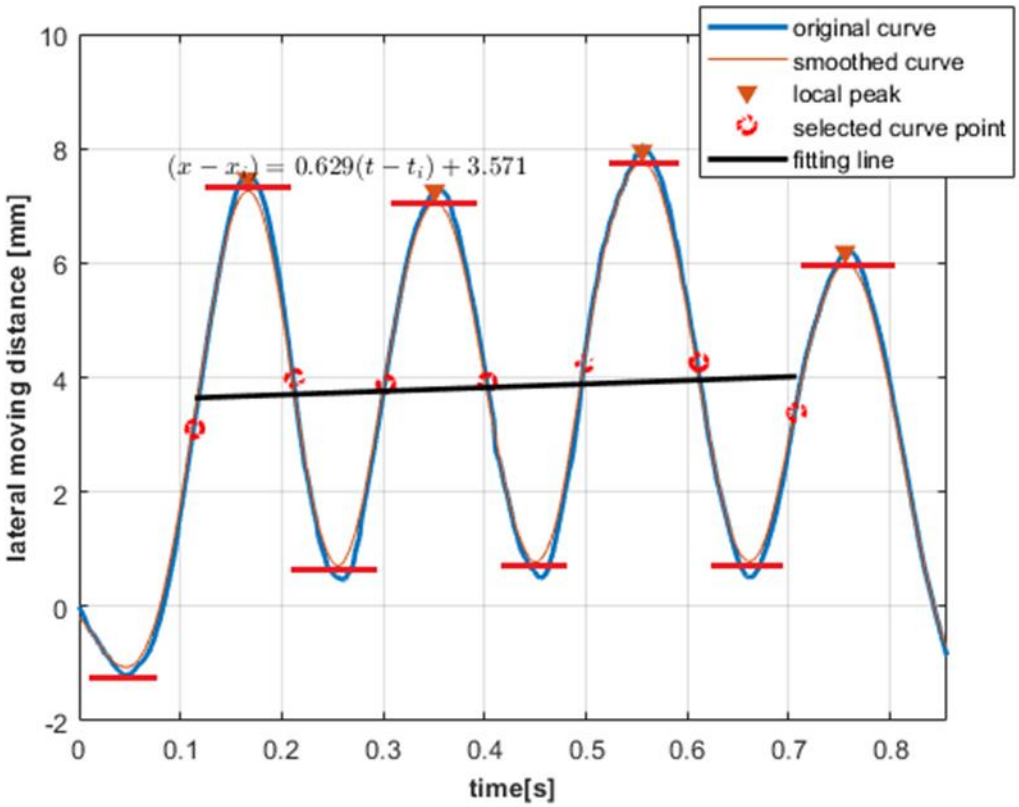

Figure 3-8: Lateral migration distance evolution with time

3.2.6 Bubble velocity

Bubble lateral and vertical instantaneous velocity are calculated as follows:

$$V_x(t) = \frac{dx}{dt} = \frac{x_{n+1} - x_n}{\Delta t} \tag{3.7}$$

$$V_z(t) = \frac{dz}{dt} = \frac{z_{n+1} - z_n}{\Delta t} \tag{3.8}$$

where (x_{n+1}, z_{n+1}) and (x_n, z_n) are the bubble center coordinate position in n+1 frame and n frame, respectively. Δt is the interval time between two frames which equals 0.002s in the condition of 500 fps. While instantaneous velocity can be calculated in this way, the average lateral velocity is obtained by linear fitting of the lateral motion displacement (Δx) versus time (Δt) as shown in. Fig.3-8. The blue curve is the original trajectory, and the red curve is the smoothed curve of the original trajectory. Rather than fitting the original trajectory, points in the middle of the oscillation

peak and valley are selected to obtain the fitting function in order to improve accuracy. The slope of the fitting line represents the lateral velocity of each bubble.

Similarly, the bubble rising velocity is obtained by linear fitting of the bubble vertical displacement Δz versus Δt as shown in Fig.3-9.

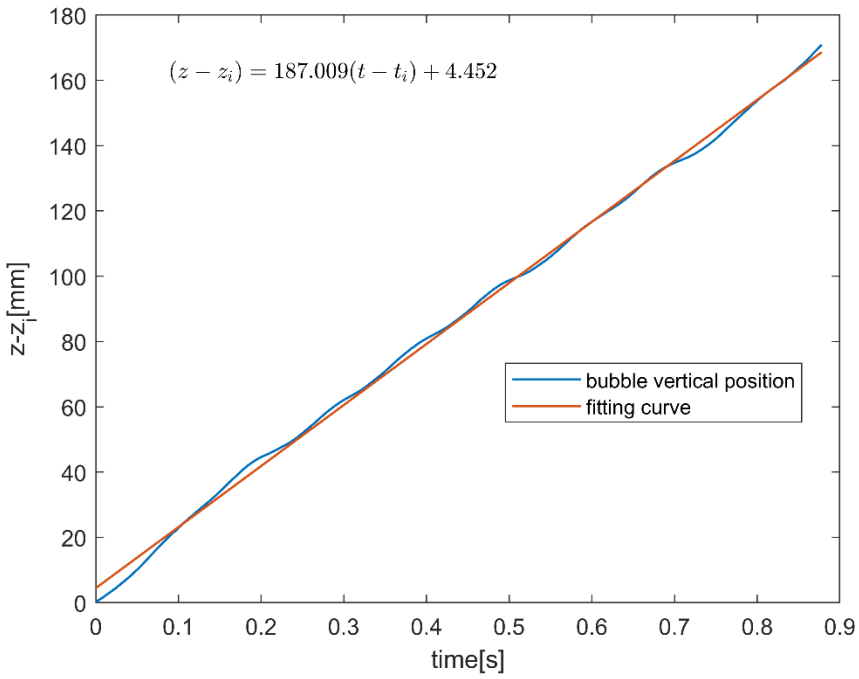

Figure 3-9: Vertical velocity fitting

It is worth to mention that the right side of the flow channel has higher downward flow velocity and resembles the center of the round pipe in downward two-phase flow, while the left side of the channel has smaller downward flow velocity and resemble the pipe wall. Bubble movement to the right side of the flow field is marked as positive velocity and vice versa.

3.2.7 Lift force calculation

The lift coefficient is obtained from force balance analysis assuming that the bubble reaches a stable state when it rises up in the observation area. Buoyant force, lift force and drag force are the three main forces acting on the bubble during its rising process in this case. As the bubble motion

is coupled with zigzag or helical motion, it is more reasonable to analyze the quasi-steady force balance by linearly fitting the trajectory of the bubble as shown in Fig.3-9.

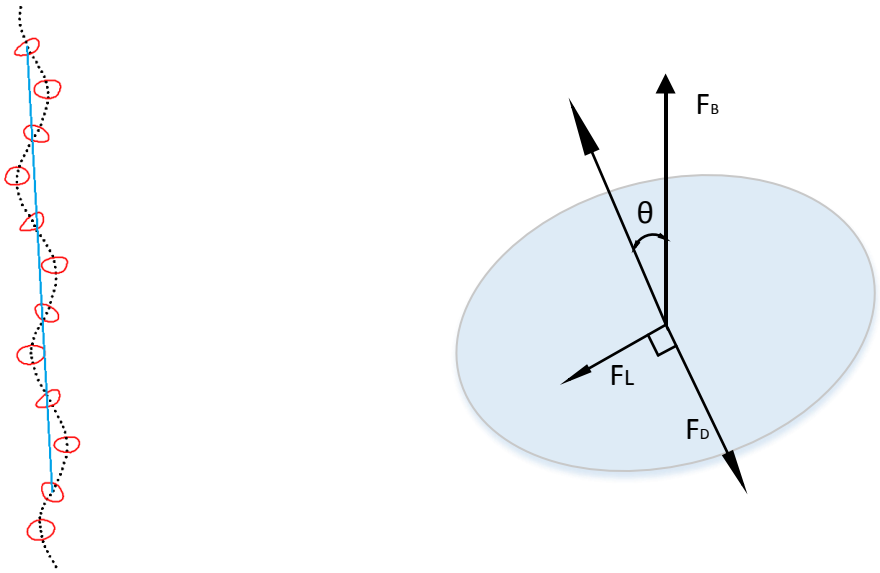

Figure 3-10: Force balance of bubble in quasi-steady state

According to Newton's Law, the force balance equation for a bubble in steady state can be expressed as:

$$0 \approx m_b \frac{d\vec{v_g}}{dt} = \sum \vec{F} = \vec{F_D} + \vec{F}_L + \vec{F_B} \tag{3.9}$$

where $\vec{F_D}$, $\vec{F_L}$, $\vec{F_B}$ are the drag force, lift force, and buoyant force, respectively. They can be expressed as:

$$\vec{F_D} = \frac{1}{2}\rho_l C_D A_g \left|\vec{v_g} - \vec{v_l}\right|(\vec{v_g} - \vec{v_l}) = \frac{\pi}{8} d_e^2 \rho_l C_D \left|\vec{v_g} - \vec{v_l}\right|(\vec{v_g} - \vec{v_l}) \tag{3.10}$$

$$\vec{F_L} = -C_L \rho_l V_r (\vec{v_g} - \vec{v_l}) \times (\nabla \times \vec{v_l}) = -\frac{\pi}{6} D_{sm}^3 \rho_l C_L (\vec{v_g} - \vec{v_l}) \times \omega \tag{3.11}$$

$$\vec{F_B} = \frac{\pi}{6} d_e^3 (\rho_l - \rho_g)\vec{g} \tag{3.12}$$

Decomposing these forces into the moving direction and normal direction, the following equations are obtained

$$\left|\vec{F_B}\right| \cdot \cos\theta = \left|\vec{F_D}\right| \tag{3.13}$$

$$\left|\overrightarrow{F_B}\right| \cdot \sin\theta = \left|\overrightarrow{F_L}\right| \tag{3.14}$$

From equation 3.10-3.14, the lift coefficient C_L is calculated as

$$C_L = \frac{\rho_l - \rho_g}{\rho_l} \frac{g \sin\theta}{(\overrightarrow{v_g} - \overrightarrow{v_l}) \times (\nabla \times \overrightarrow{v_l})} = \frac{\rho_l - \rho_g}{\rho_l} \frac{g}{(\overrightarrow{v_g} - \overrightarrow{v_l}) \times (\nabla \times \overrightarrow{v_l})} \frac{\left|\overrightarrow{v_g} - \overrightarrow{v_l}\right|_x}{(\overrightarrow{v_g} - \overrightarrow{v_l})} \tag{3.15}$$

The expression is simplified by taking $\frac{\rho_l - \rho_g}{\rho_l} \approx 1$

$$C_L = \frac{g}{\omega} \frac{\left|\overrightarrow{v_g} - \overrightarrow{v_l}\right|_x}{\left|(\overrightarrow{v_g} - \overrightarrow{v_l})\right|^2} \tag{3.16}$$

The shear rate magnitude, lateral migration velocity and relative velocity of the bubble are three major parameters that determined the value of the lift coefficient, and they are obtained as discussed in previous sections.

3.2.8 Uncertainty analysis

Various uncertainties exist in the measurement procedures. The benchmark is around 1.8% under the current experimental setup. For bubble edge detection, the maximum error is caused by the blurred edge of the bubble. The uncertainty caused by this factor is within 10% when the bubble diameter exceeds 3mm and keeps decreasing with bubble size. Another uncertainty comes from the deformation of the bubbles. In terms of large bubbles, the uncertainty of its equivalent diameter grows as the shape become more irregular. Comparison of bubble size is made between the value obtained from the image processing and the calculation based on the volume of injected air. The greatest uncertainty found for large bubbles with d_e =10mm is around 10%. The error grows with increasing bubble diameter as its shape become more irregular; however, the greatest error is no more than 20% for the largest bubble measured in this experiment.

CHAPTER 4. RESULTS ANALYSIS

This chapter mainly discusses the experiment results in four aspects, which are terminal velocity, oscillation amplitude, aspect ratio and lift force coefficient.

Bubbles with equivalent diameter ranging from 3mm to 8mm are generated with different-sized needles. Bubbles with diameter larger than 8mm are released by rotating the spoon. For small bubbles generated by the needles, bubbles of similar size are repeatedly generated 30-35 times in order to analyze their motion characteristics statistically.

4.1 Terminal velocity evaluation

4.1.1 Instantaneous velocity evaluation

Although the bubble reaches steady state after rising a specific distance, the terminal velocity does not stay constant but fluctuates during the rising process. The value depends on the deformation and size of the bubble. Fig.4-1 shows typical trajectories of bubbles with d_e =3.52mm, 3.95mm, 5.51mm, 6.23mm, 9.27mm and 16.87mm. Corresponding instantaneous horizontal and vertical velocities and aspect ratio are presented in Fig. 4-2 and Fig.4-3. Small bubbles with small initial deformation rise up with zigzag motion. With increasing bubble size to around 5.51mm, the oscillation amplitude decreases. However, the oscillation amplitude increases again when the bubble size is larger than 5.51mm. Instantaneous vertical velocity, horizontal velocity and aspect ratio show periodic fluctuation when the bubble size is relative small. With increasing bubble size, periodic oscillation still exists in the vertical and horizontal velocities; however, it becomes more unstable and chaotic as shown in Fig.4-2. For all the bubbles investigated, the fluctuation frequency of V_z is twice of V_x. V_z reaches minimum value when V_x reach its absolute maximum value. V_z reaches its maximum value when V_x equals 0. This phenomenon is consistent with the experiment results of Lunde and Perkin (Fascination & Fluid, 1998), Tomiyama et al.(A. Tomiyama et al., 2002) and Li et al.(Li, Zhao, et al., 2016). Oscillation behavior is less prominent for intermediate-sized bubbles with large initial deformation. In addition, with increasing size, bubbles aspect ratio decreases and V_x , V_z show less periodic motion compared to small bubbles.

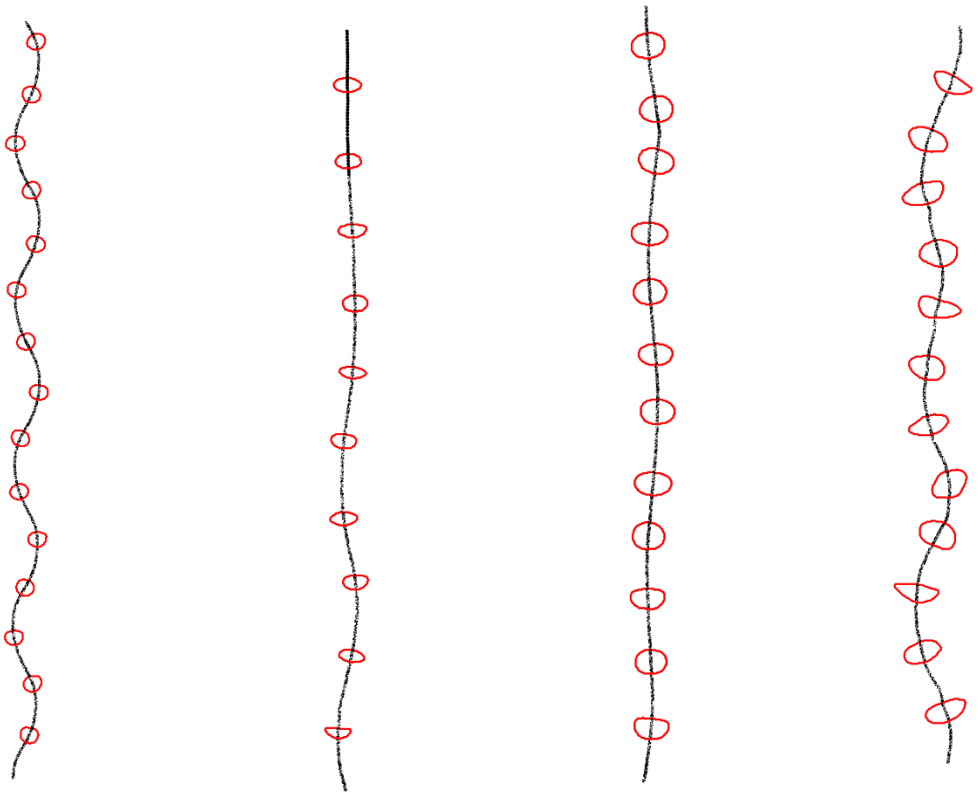

(a) ID=1.07mm d_e =3.52mm | (b) ID=2.69mm d_e =3.95mm | (c) ID=3.81mm d_e =5.51mm | (d) ID=3mm d_e =6.23mm

Figure 4-1: Trajectory of different size bubble generated by different size needles or by rotating spoon

Figure 4-1 continued

(e) Released by spoon
d_e =9.27mm

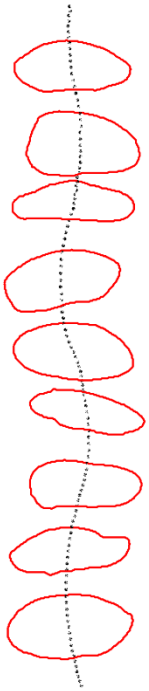

(f) Released by spoon
d_e =16.87mm

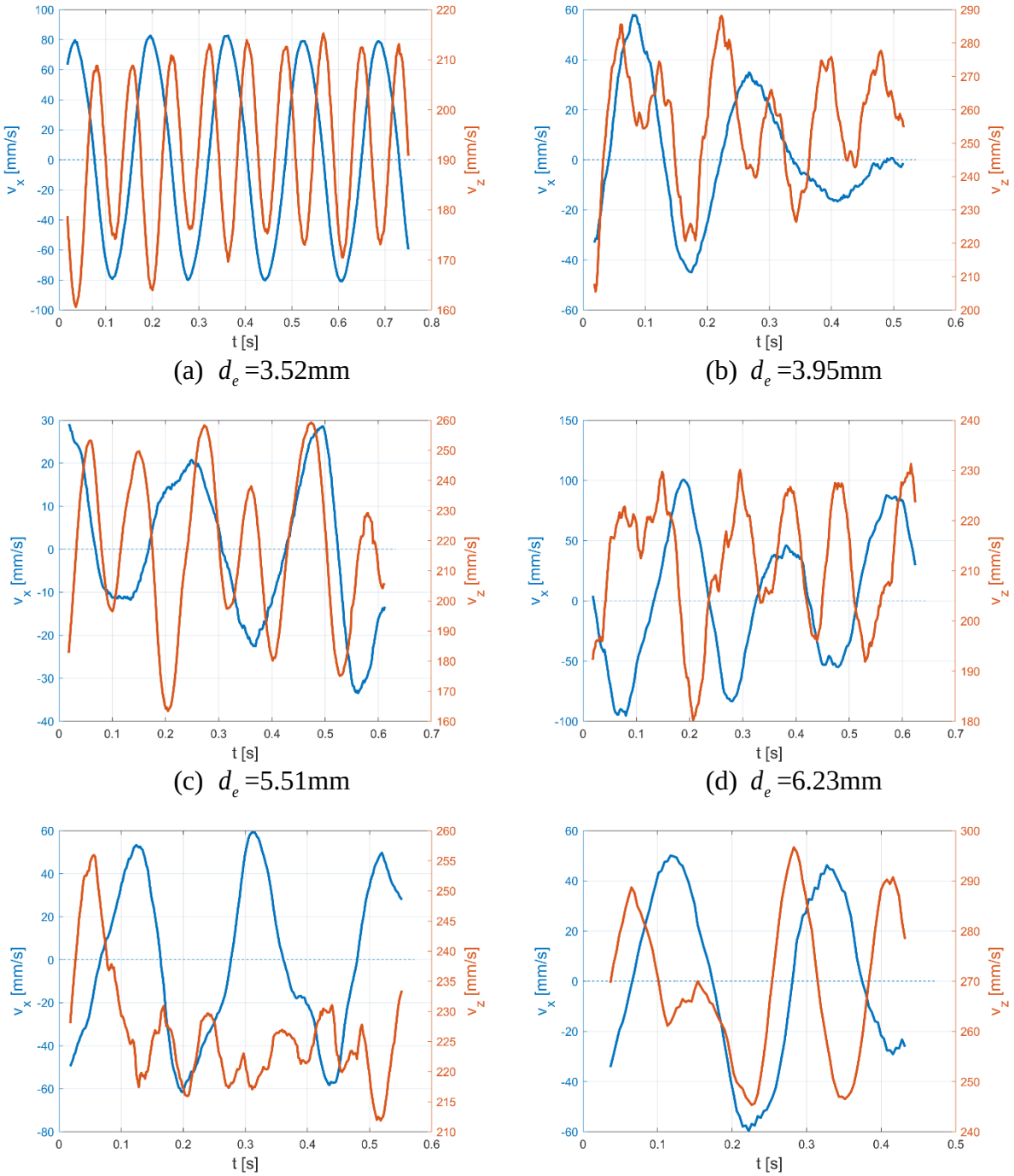

(a) d_e =3.52mm (b) d_e =3.95mm

(c) d_e =5.51mm (d) d_e =6.23mm

(e) d_e =9.27mm (f) d_e =16.87mm

Figure 4-2: Horizontal and vertical velocity evolution of different size bubble

Fig. 4-3 presents the bubble vertical velocity and aspect ratio evolution with time. The terminal velocity model proposed by Tomiyama et al. (A. Tomiyama et al., 2002) is also compared. The bubble rising velocity is found to be strongly dependents upon the aspect ratio. The bubble

instantaneous velocity reaches local peak or local valley when the aspect ratio reaches minimum value or maximum value. This dependence is prominent for small bubbles; it is less prominent when the bubble size is large and the aspect ratio is smaller than 0.5 as shown in Fig.4-3(f). The model tracks the fluctuation of rising velocity well when the bubble aspect ratio is large than 0.6. However, the prediction becomes worse with decreasing aspect ratio.

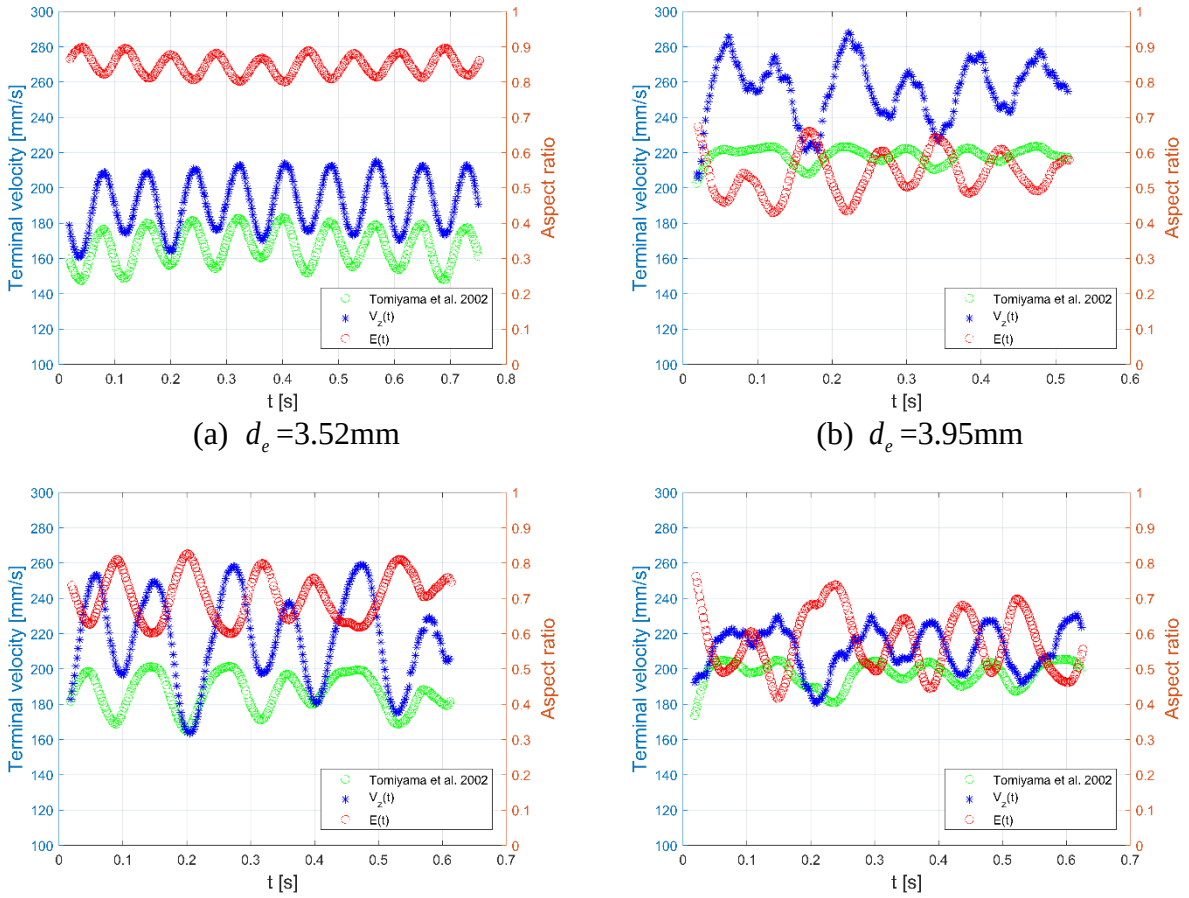

(a) d_e =3.52mm (b) d_e =3.95mm

(c) d_e =5.51mm (d) d_e =6.23mm

Figure 4-3: Vertical velocity and aspect ratio evolution of different size bubble

Figure 4-3 continued

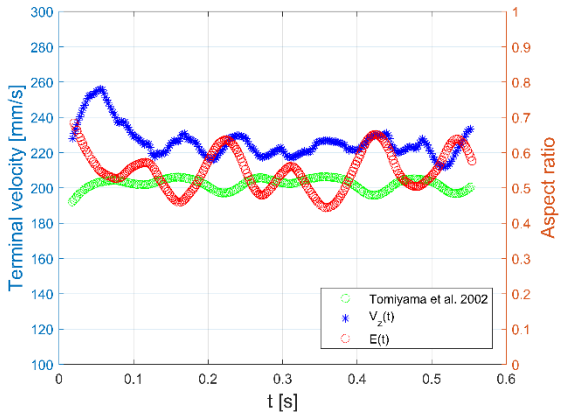

(e) d_e =9.27mm

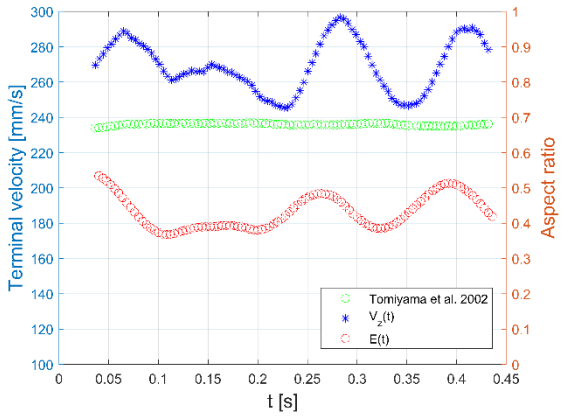

(f) d_e =16.87mm

4.1.2 Terminal velocity evaluation

Terminal velocity of different-sized bubbles from 2mm to 20mm has been investigated. Fig. 4-4 shows bubble terminal velocity versus bubble size in this experiment and comparison with the prediction of existing models. The terminal velocity is obtained through linear fitting of bubble trajectory as shown in Fig.3-9.

Clift et al.(Clift, Grace, & Weber, 2005) measured bubble terminal velocity in water of different quality at 20°C. Bubble equivalent diameter ranges from 0.2mm to 40mm, and *Eo* number ranges from 0.01 to 200. It was found that the water quality has significant effect on small bubble terminal velocity. In contaminated water, terminal velocity monotonically increases with bubble diameter. While in pure water, the bubble terminal velocity reaches peak value with diameter between 1mm and 2mm; thereafter, it decreases until the bubble equivalent diameter reaches around 6mm and then increases again with increasing diameter.

Although lacking the data for bubble smaller than 2mm, a decreasing trend of the upper bound of the terminal velocity is observed in the current experiment data for bubbles between 2mm to 6mm as shown in Fig.4-4, which agrees well with Clift's data (Clift et al., 2005). The agreement indicates that the water used in this experiment can be treated as pure water and there is no contamination effect on bubble motion. The scatted data is attributed to the initial deformation of

the bubble rather than water contamination as indicated by Wu et al. (Wu & Gharib, 2002) and Tomiyama et al.(A. Tomiyama et al., 2002).

In prediction of the bubble terminal velocity in the fluid, Mendelson et al.(Mendelson, 1967) made progress on theoretical understanding of bubble motion by applying wave theory and assuming the bubbles' motion in inviscid fluid as merely interfacial disturbance. Wave velocity was first proposed by Lamb (Lamb, 1993) as follows:

$$V_T = \sqrt{\frac{2\pi\sigma}{\lambda(\rho_L + \rho_G)} + \frac{g\lambda}{2\pi}} \tag{4.1}$$

The wavelength is later specified as $\lambda = \pi d_e$ by Mendelson (Mendelson, 1967) and terminal velocity of the bubble is given as:

$$V_T = \sqrt{\frac{2\sigma}{d_e(\rho_L + \rho_G)} + \frac{gd_e}{2}} \tag{4.2}$$

For bubbles with larger diameter from 6mm to 19mm. this model slightly over-predicts the terminal velocity and the discrepancy between prediction and experiment data becomes more pronounced as bubble size increases.

Peebles (Peebles, 1953) correlated bubble terminal velocity with Reynolds number, *Eo* number and Weber number and proposed a drag correlation as:

$$C_D = \max\{\max[\frac{24}{\mathrm{Re}}, \frac{18.7}{\mathrm{Re}^{0.68}}], \min[0.0275EoWe^2, 0.82Eo^{0.25}We^{0.5}]\} \tag{4.3}$$

This model over-predicts the bubble terminal velocity in the range from 2mm to 14mm and underestimates the velocity for bubbles with diameter larger than 14mm.

Schiller and Naumann (Schiller & Naumann, 1933) conducted simulation and assumed there was no deformation of bubbles. A correlation for drag coefficient based on simulation results was proposed as:

$$\begin{aligned} C_D &= \frac{24(1+0.15\,\mathrm{Re}^{0.687})}{\mathrm{Re}} \quad (\mathrm{Re} \le 1000) \\ C_D &= 0.44 \quad (\mathrm{Re}>1000) \end{aligned} \tag{4.4}$$

The model has good prediction for bubbles smaller than 2mm; however, it rises to much high value beyond the normal range.

Levich et al. (Levich, 1962) and Schiller et al.'s model (Schiller & Naumann, 1933) prediction increases rapidly for small bubbles and deviates from the experiment data for large bubbles. Thus, this model is not valid in the large bubble region.

Tomiyama et al. (TOMIYAMA, KATAOKA, ZUN, & SAKAGUCHI, 1998) took bubble deformation, size and fluid properties into account when they proposed the model. A new drag coefficient model for drag in a pure system was proposed as:

$$C_D = \xi \max[\min\{\frac{16}{\mathrm{Re}}(1+0.15\mathrm{Re}^{0.687}), \frac{48}{\mathrm{Re}}\}, \frac{8}{3}\frac{Eo}{Eo+4}] \tag{4.5}$$

$$10^{-2} < Eo < 10^{3};$$
$$10^{-14} < Mo < 10^{7};$$
$$10^{-3} < \mathrm{Re} < 10^{5}$$

where ξ is tuning factor to make the correlation best fit the experiment data.

Ishii and Chawla (Maki Ishii & Chawla, 1979) gave a general correlation for drag coefficient in wide Reynolds number ranges from Stokes regime up to Newton's regime as:

$$C_D = \max\left\{\frac{24}{\mathrm{Re}}(1+0.1\mathrm{Re}^{0.75}), \min[\frac{2}{3}\sqrt{Eo}, \frac{8}{3}]\right\} \tag{4.6}$$

This model also related the bubble's Reynolds number and *Eo* number. It well predicts the bubble with diameter larger than 8mm, but, does not reflects the terminal velocity of small bubbles with different aspect ratio.

Wallis (Wallis, 1974) proposed the drag coefficient as:

$$C_D = \max\{\min[\max(\frac{16}{\mathrm{Re}}, \frac{13.6}{\mathrm{Re}^{0.8}}), \frac{48}{\mathrm{Re}}], \min[\frac{Eo}{3}, 0.47Eo^{0.25}We^{0.5}, \frac{8}{3}]\} \tag{4.7}$$

Prediction of this model has similar trend with experiment data, but, slightly over-predicts the velocity for bubble with diameter from 2mm to 5mm and for bubbles with diameter larger than 14mm.

All the models mentioned above ignored deformation of bubble. Tomiyama (A. Tomiyama et al., 2002) proposed a terminal velocity model of bubble under the surface dominate regime by taking account of the aspect ratio. The bubbles were assumed to be symmetric spheroidal. In consideration of surface tension effect and to extend the potential flow analysis of a sphere to bubble, the terminal velocity is expressed as:

$$V_T = \frac{\sin^{-1}\sqrt{1-E^2} - E\sqrt{1-E^2}}{1-E^2}\sqrt{\frac{8\sigma}{\rho_L d}E^{4/3} + \frac{\Delta\rho g d}{2\rho_L}\frac{E^{2/3}}{1-E^2}} \tag{4.8}$$

It clearly shows in Fig.4-4 that this model has the best trend prediction of bubble's terminal velocity even for the scattered value of small bubbles.

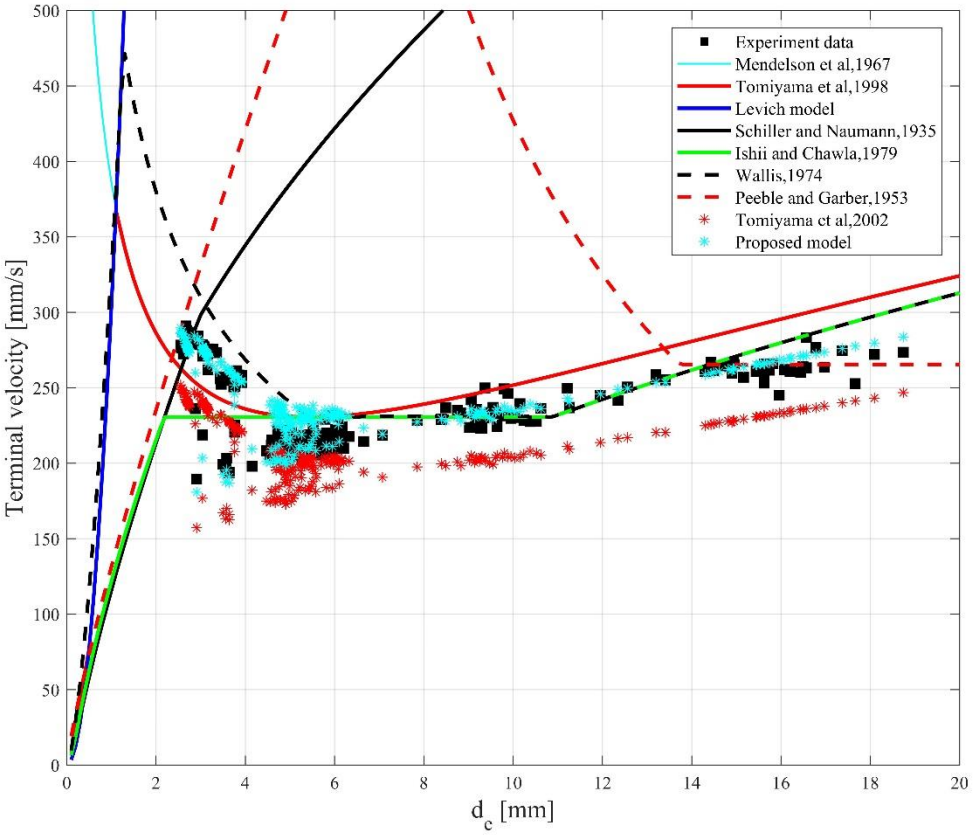

Figure 4-4: Terminal velocity of bubble in stagnant water

In addition, the model correlated with the aspect ratio can reflect the fluctuating instantaneous velocity of bubbles due to zigzag or helical motion. Fig 4-5 shows a bubble with d_e =3.41mm rising up in stagnant water. The instantaneous terminal velocity depends strongly upon the bubble aspect ratio. As shown in Fig.4-5, terminal velocity reaches local peak while aspect ratio reaches minimum value.

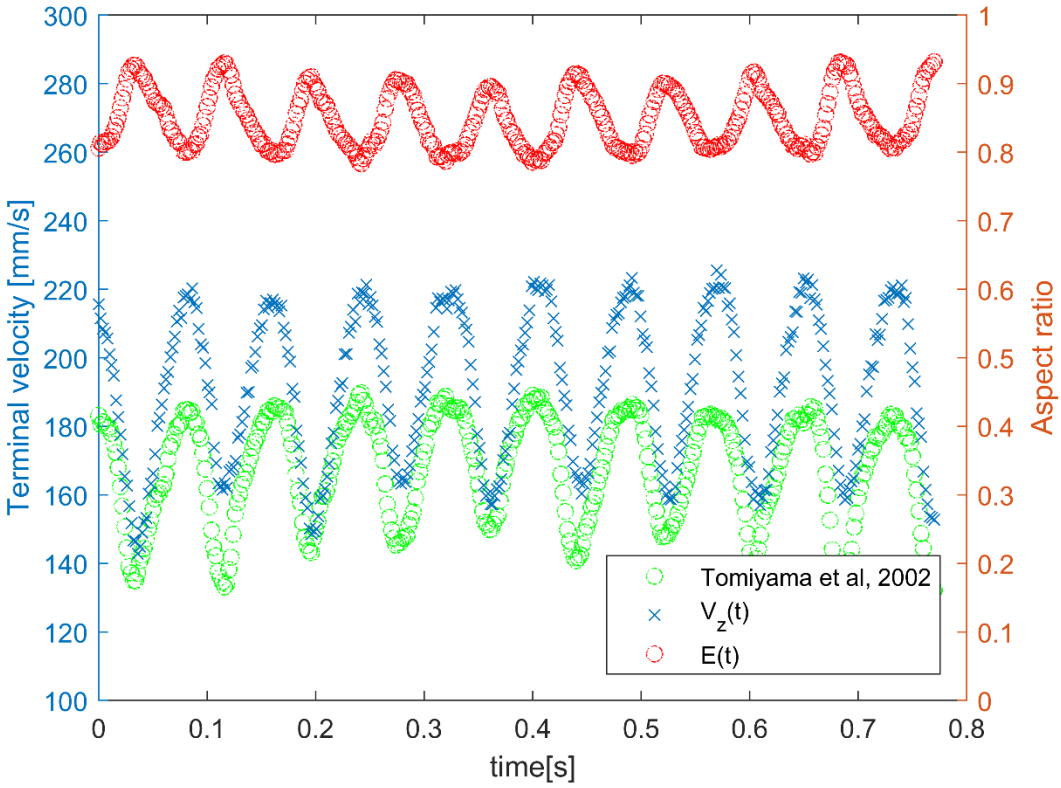

Figure 4-5: Terminal velocity and aspect ratio evolution in stagnant water

Due to the asymmetric deformation of bubble, the experimental data is slightly greater than the prediction of Tomiyama's model (A. Tomiyama et al., 2002). Thus a tuning factor $\varepsilon = 1.15$ is added to his model to best fit the experiment data. The proposed model has the best prediction of current experiment data in the range of all bubble size, but with only a slight over-prediction of the terminal velocity for bubbles in 4mm-6mm.

$$V_T = \varepsilon \cdot \frac{\sin^{-1}\sqrt{1-E^2} - E\sqrt{1-E^2}}{1-E^2} \sqrt{\frac{8\sigma}{\rho_L d} E^{4/3} + \frac{\Delta\rho g d}{2\rho_L} \frac{E^{2/3}}{1-E^2}} \tag{4.9}$$

4.2 Bubble oscillation amplitude analysis

It is observed that all the bubbles in this study rose up with zigzag and helical motion as many researchers indicated. Okawa et al.(Okawa, Tanaka, Kataoka, & Mori, 2003), Wu et al. (Wu & Gharib, 2002) and Tsuge et al. (Tsuge & Hibino, 1977) found that bubble tend to have rectilinear motion when its equivalent diameter is sufficiently small. The zigzag or helical motion appears with the increase in size. Okawa et al.(Okawa et al., 2003) investigated bubble oscillation in stagnant distilled water and correlated bubbles's dimensionless oscillation amplitude with their Reynolds number and Strouhal number. They pointed out that the dimensionless amplitude is small when the bubble Reynolds number is close to the onset of oscillation, which is set to 450 according to experimental data. The proposed model of oscillation amplitude is

$$O_s = d_e C_R St^{-1} \tag{4.10}$$

where $St = 0.1 C_D^{0.734}$ is given by Tsuge (Tsuge & Hibino, 1977) and $C_R = 0.1 \times \{1 - e^{-0.0061(\mathrm{Re} - \mathrm{Re}_C)}\}$.

Fig. 4-6 compares the oscillation amplitude of bubbles of various equivalent diameter in the current experiment with Okawa's model (Okawa et al., 2003). Oscillation amplitudes in three different flow conditions show similar results. The upper bound of oscillation decreases from 10mm to 5mm as the bubble equivalent diameter increases from 3mm to 10mm. The lower bound of amplitude slightly increases in this range. Bubble with diameter over 14mm oscillate wider than bubbles in the intermediate size from 8mm to 12mm. Okawa's prediction is within the experimental data range for bubbles between 3mm to 6mm and agrees with the upper bound of experiment data for large bubble. The widely scattered characteristic of bubble oscillation coincide with the wide scattered aspect ratio, thus the correlation of oscillation amplitude may need to take aspect ratio into consideration. However, in the current stage, it would be difficult to incorporate them in one correlation. The data obtained would be useful for further development.

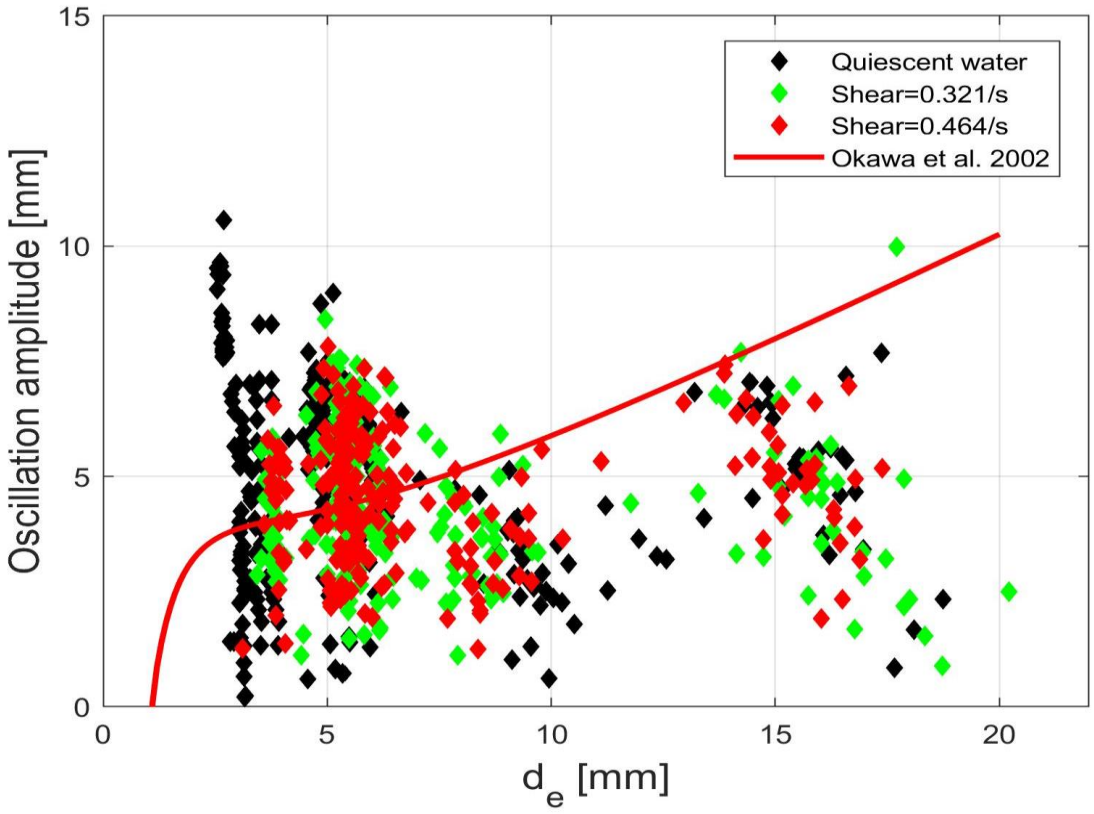

Figure 4-6: Bubble oscillation amplitude in stagnant water and weak shear flow

Fig.4-7 provides oscillation amplitude of bubble with different sizes generated by different needles in stagnant water and shear flow

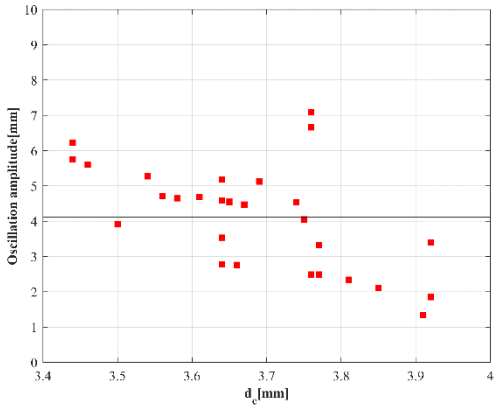

(1) ID=1.07mm, $\omega = 0$

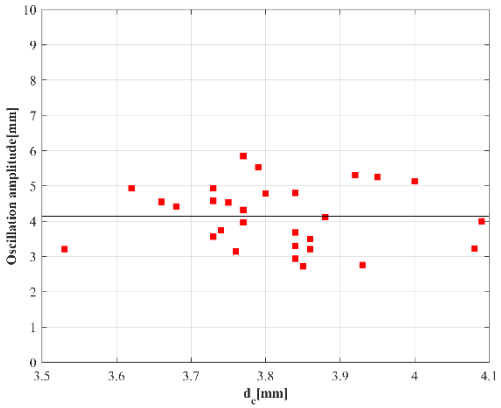

(2) ID=1.07mm, $\omega = 0.321/s$

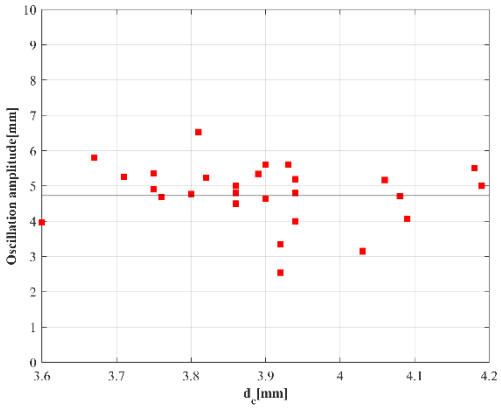

(3) ID=1.07mm, $\omega = 0.464/s$

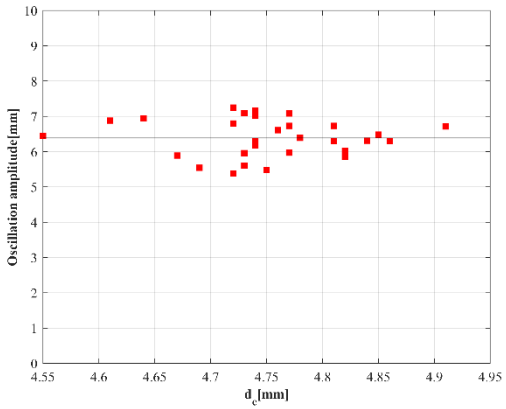

(4) ID=2.69mm, $\omega = 0$

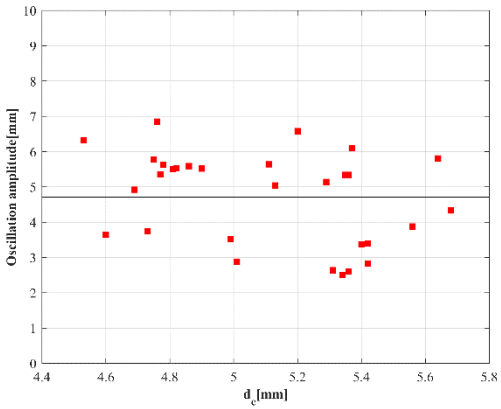

(5) ID=2.69mm, $\omega = 0.321/s$

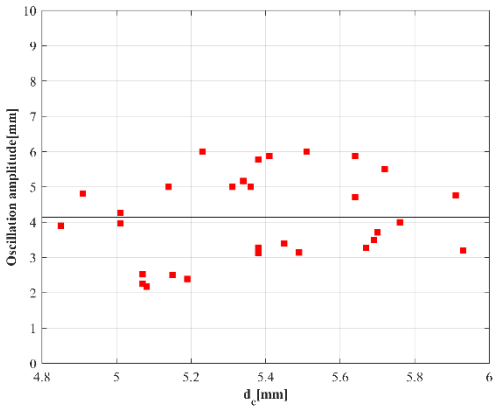

(6) ID=2.69mm, $\omega = 0.464/s$

Figure 4-7: Oscillation amplitude of different size bubble generated by various size needles

Fig. 4-7 continued

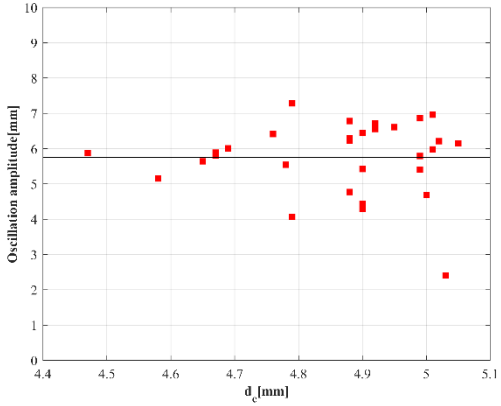

(7) ID=3mm, $\omega = 0$

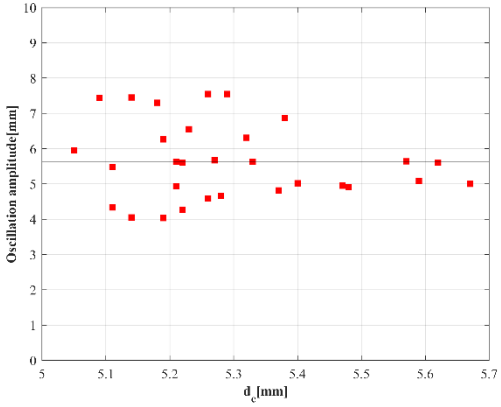

(8) ID=3mm, $\omega = 0.321/s$

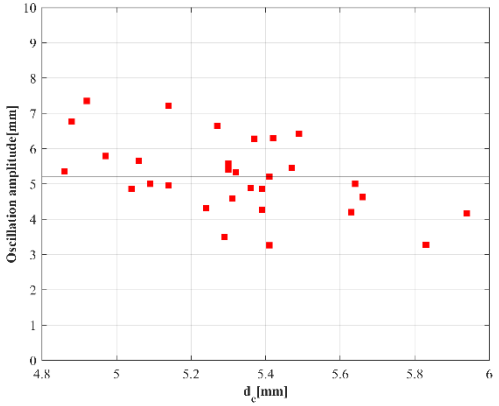

(9) ID=3mm, $\omega = 0.464/s$

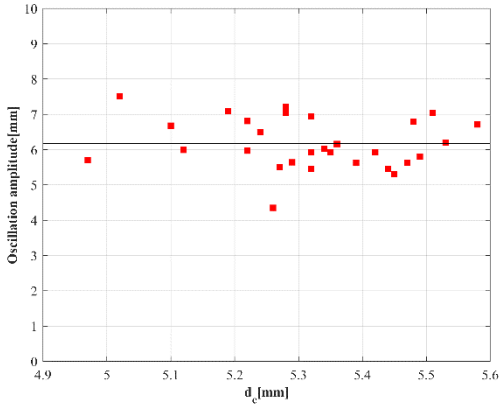

(10) ID=3.81mm, $\omega = 0$

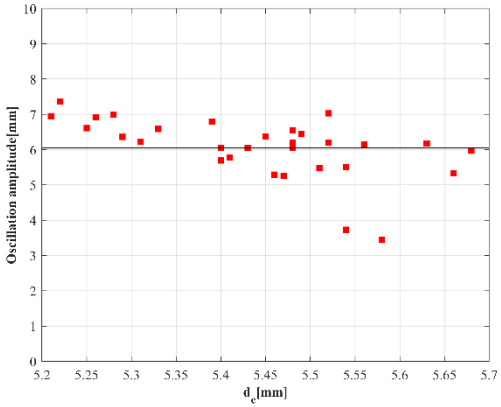

(11) ID=3.81mm, $\omega = 0.321/s$

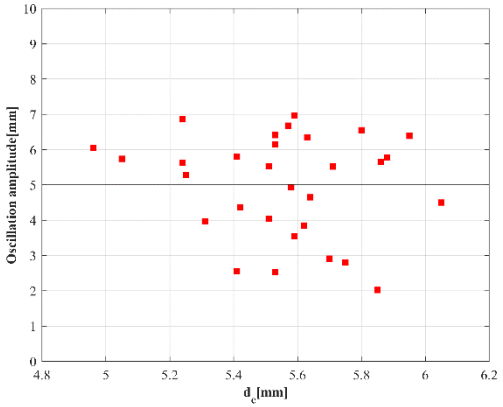

(12) ID=3.81mm, $\omega = 0.464/s$

Fig. 4-7 continued

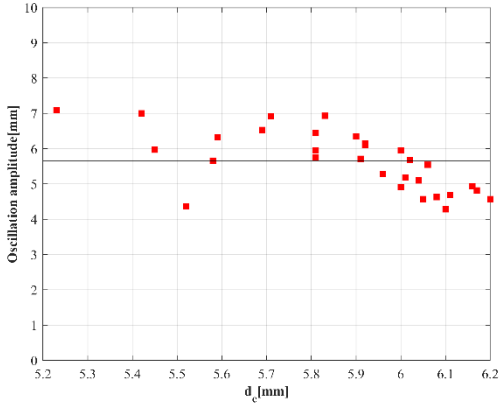

(13) ID=4.8mm, $\omega = 0$

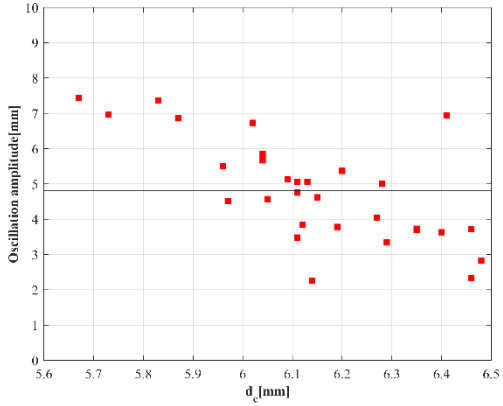

(14) ID=4.8mm, $\omega = 0.321/s$

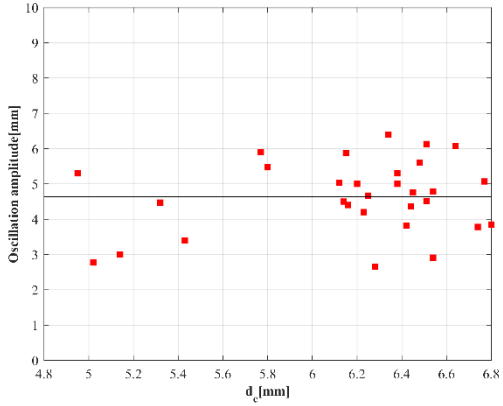

(15) ID=4.8mm, $\omega = 0.464/s$

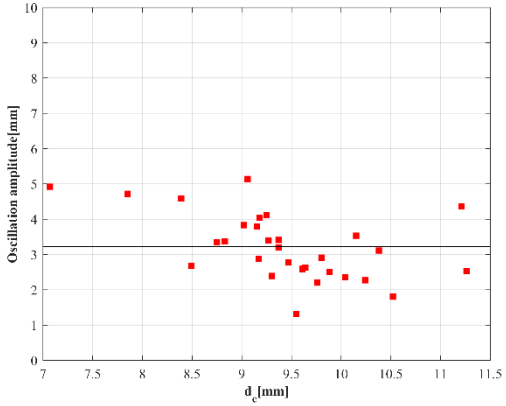

(16) Released by spoon , $\omega = 0$

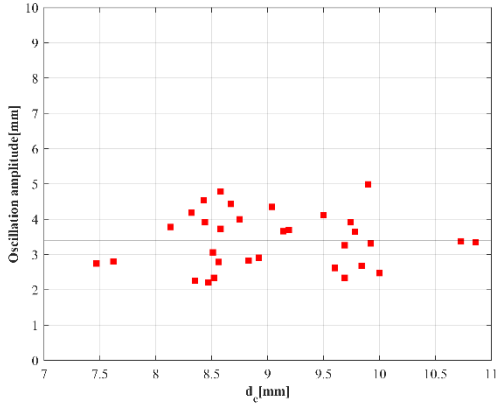

(17) Released by spoon, $\omega = 0.321/s$

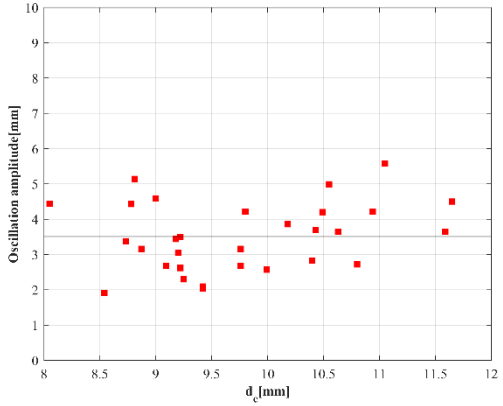

(18) Released by spoon, $\omega = 0.464/s$

Fig. 4-7 continued

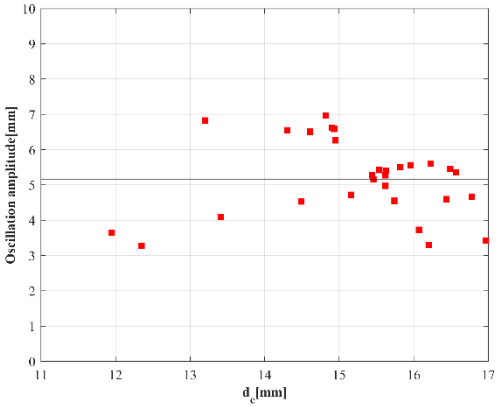

(19) Released by spoon, $\omega = 0$

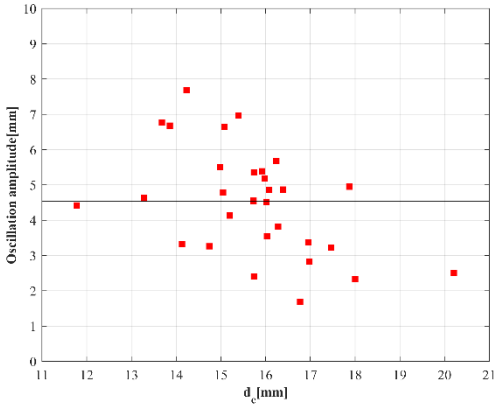

(20) Released by spoon, $\omega = 0.321/s$

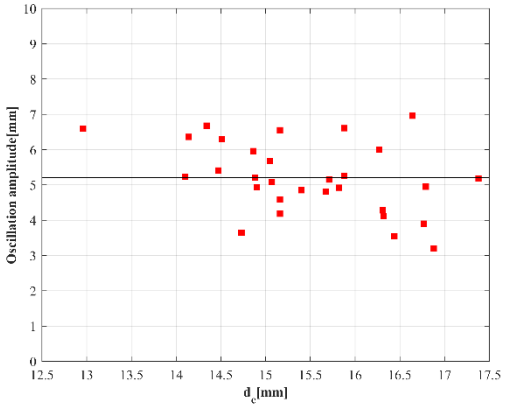

(21) Released by spoon, $\omega = 0.464/s$

4.3 Bubble aspect ratio evaluation

Bubble terminal velocity strongly depends on its aspect ratio as discussed in the previous section. Thus, accurately prediction of bubble aspect ratio is important in prediction of terminal velocity.

Fig.4-8 and Fig. 4-9 show the aspect ratio of various-sized bubbles under different flow conditions. Bubble aspect ratio shows similar trend both in stagnant water and low linear shear flow. For small bubbles, the aspect ratio value varies from 0.5 to 0.9 due to the different sizes of needles. Bubbles from 2mm to 7mm were generated by needles. Small needles generate large initial deformation while large needles generate small initial deformation bubble. Nevertheless, the upper bound of the aspect ratio keeps decreasing as bubble size grows. It is interesting to point out that the lower bound of the aspect ratio stays at a constant value around 0.5 while the upper bound of the aspect ratio decreases from 0.9 to 0.75. For larger bubbles released by the rotating spoon, the data is less scattered and keep decreasing with bubble size.

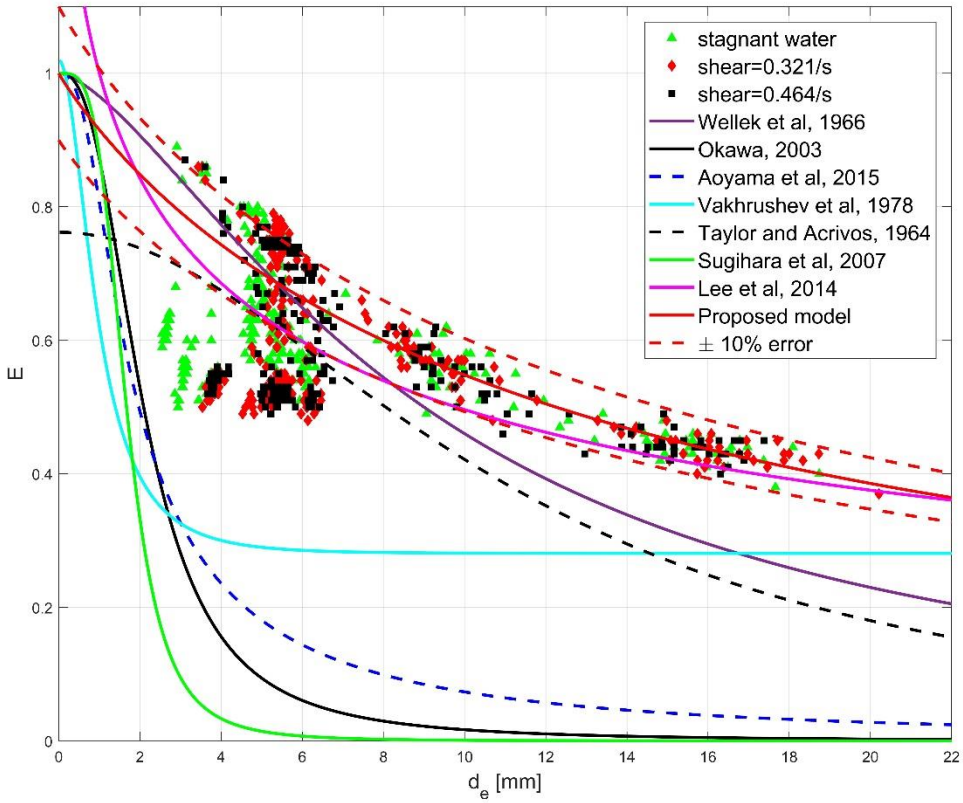

Figure 4-8: Bubble aspect ratio versus equivalent diameter

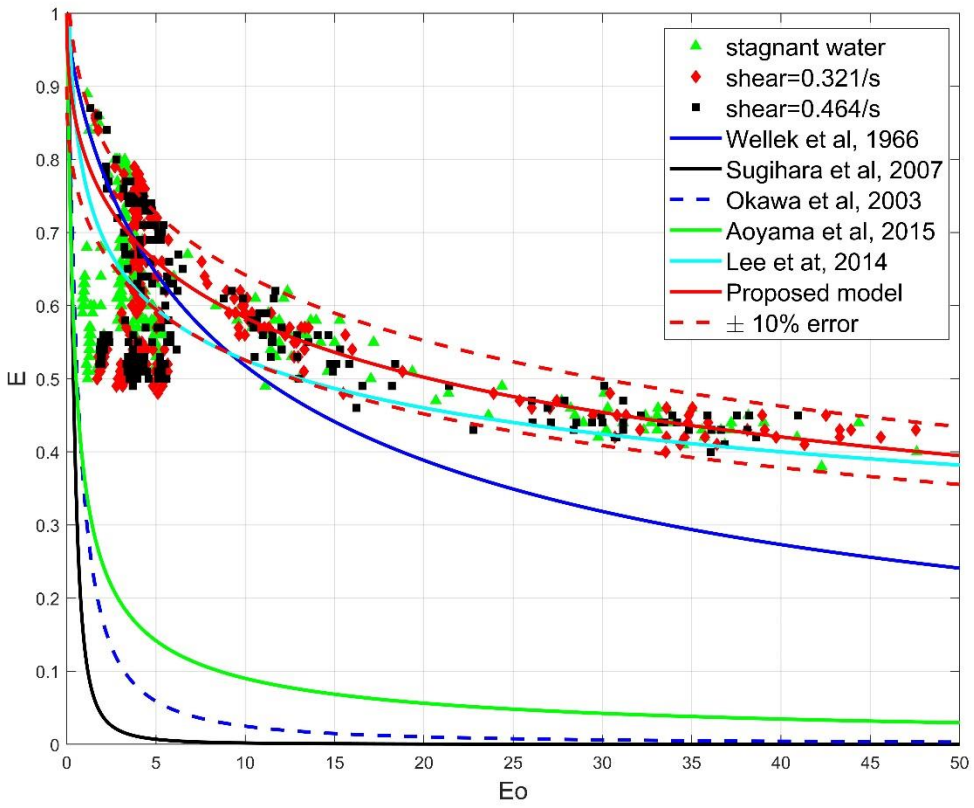

Figure 4-9: Bubble aspect ratio versus *Eo* number

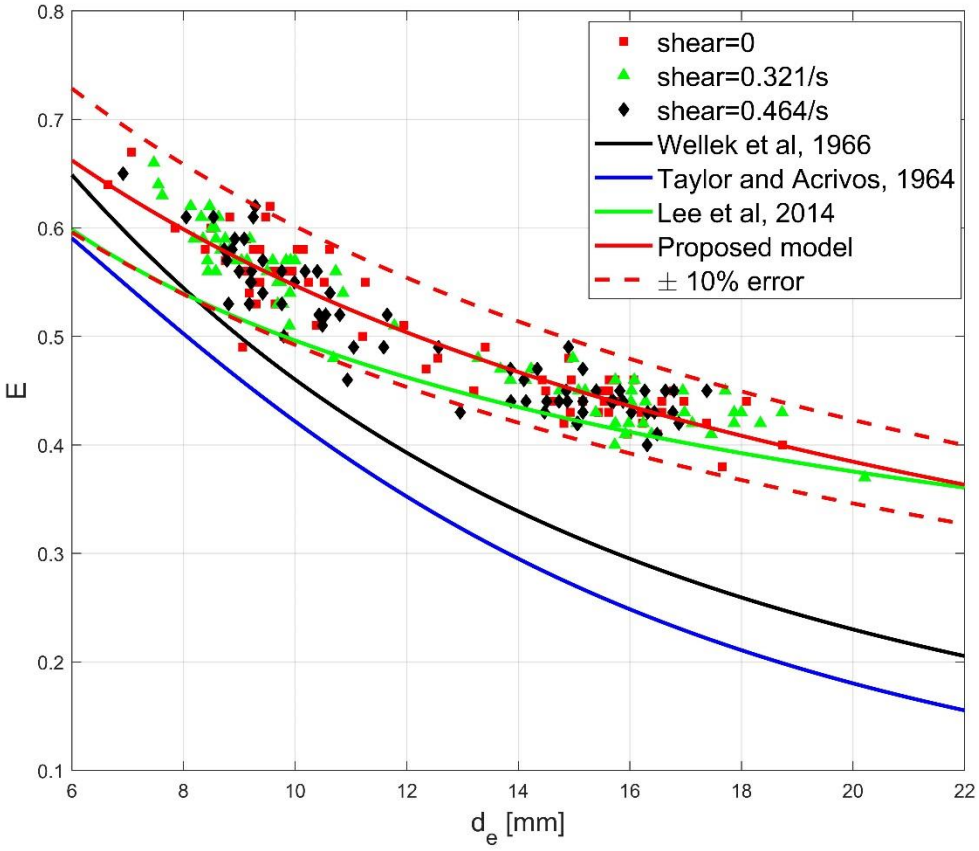

Figure 4-10: Bubble aspect ratio versus equivalent diameter in large size region

In terms of existing models' prediction of aspect ratio, Taylor and Acrivos (Taylor & Acrivos, 1964) correlated aspect ratio with Weber number as:

$$E = \frac{1}{1+\frac{5}{32}We} \tag{4.11}$$

This model underestimates the aspect ratio for bubbles larger than 7mm.

Wellek et al. (Wellek, Agrawal, & Skelland, 1966) proposed a model to predict droplet aspect ratio in fluid from non-oscillating drops falling or rising in stationary liquid. The correlation was proposed as:

$$E = \frac{1}{1+0.163Eo^{0.757}} \tag{4.12}$$

Wellek's model has similar trend prediction to the experimental data but underestimates the aspect ratio of bubbles with large diameter, declining to small value below 0.4.

Okawa (Okawa et al., 2003) noticed that Wellek's model (Wellek et al., 1966) provides reasonable prediction of aspect ratio for smaller bubbled and agreed with its upper boundary. A new correlation is recommended for the lower boundary of aspect ratio of small bubble as:

$$E = \frac{1}{1+1.97Eo^{1.3}} \tag{4.13}$$

It agrees well with the experiment data in conditions where *Eo* <1; however, it deviates from experiment data for large bubbles.

Sugihara et al. (Sugihara, Sanada, Shirota, & Watanabe, 2007) conducted experiments in super clean water and gave a correlation as:

$$E = \frac{1}{1+6.5Eo^{1.925}} \tag{4.14}$$

Lee et al.(Lee & Choi, 2014.) conducted experiment for large bubble in shear flow and observed that Wellek's model (Wellek et al., 1966) underestimated the aspect ratio for larger bubbles and suggested a new correlation as:

$$E = \frac{1.7}{1+1.2Eo^{0.27}} \tag{4.15}$$

This model has the best trend prediction among the existing models. However, it slightly under estimates the aspect ratio for large bubbles and overestimates it when the bubble size is extremely small.

Aoyama et al. (Aoyama, Hayashi, Hosokawa, & Tomiyama, 2016) proposed an empirical aspect ratio model based on the experiment of ellipsoidal bubbles rising in highly viscous fluid. The aspect ratio model is correlated with the *Eo* number and the bubble Reynolds number as:

$$E = \frac{1}{[1+0.016Eo^{1.12}\,\mathrm{Re}]^{0.388}} \tag{4.16}$$

This correlation is extended to fluid with much lower viscosity to $\log M = -11$ and shows good agreement with their experiment data and Sugihara's data for d_e from 0 to 8mm.

After reviewing all the models and experiment data, it would be difficult to give a good model for small bubbles as their aspect ratio data scatter widely. However, the scatter of aspect ratio of large bubbles is small, and a new correlation better reflecting the experiment data for large bubble is proposed as:

$$E = \frac{1}{1 + 0.239 Eo^{0.475}} \tag{4.17}$$

The proposed model has good agreement with experiment data in the large bubble region and is valid in both quiescent water and weak shear flow field. Almost all the experiment data for bubbles larger than 6mm fall inside the ±10% error bound of this model. The smallest bubble aspect ratio for the air-water system approaches approximately 0.4 as shown in the experiment. This aspect ratio limit agrees with simulation results obtained by W.Dijkhuizen (Dijkhuizen et al., 2010) when bubbles are large enough.

Fig.4-11 below shows the aspect ratio of different-sized bubbles in different shear rate magnitude.

.

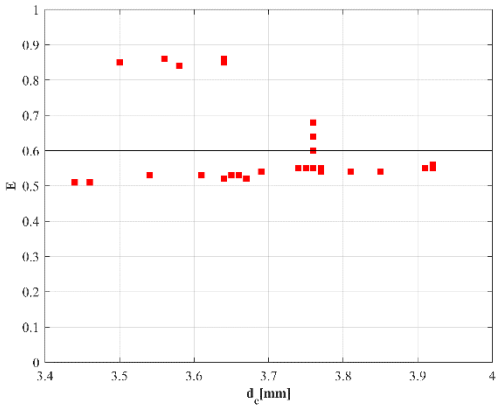

a) ID 1.07mm, $\omega = 0$

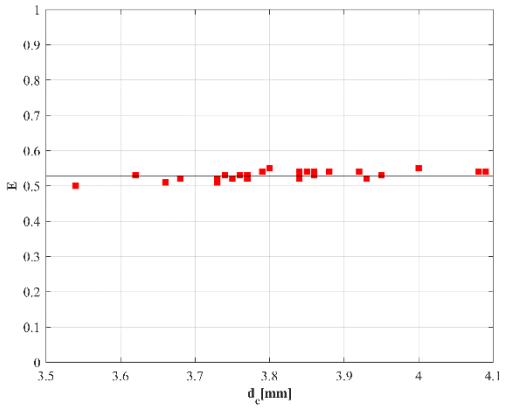

b) ID 1.07mm, $\omega = 0.321/s$

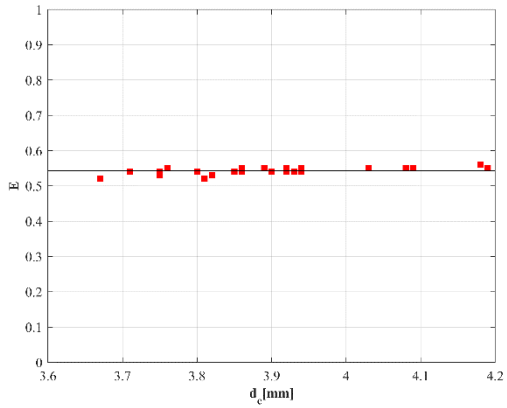

c) ID 1.07mm, $\omega = 0.464/s$

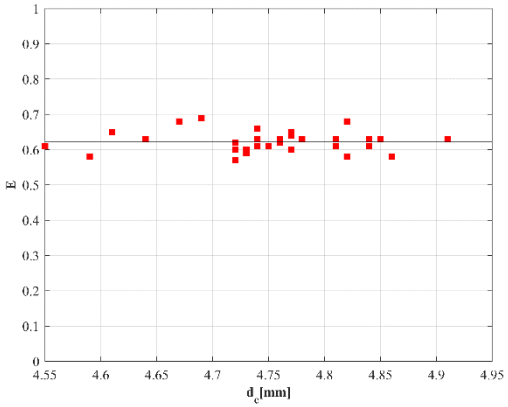

d) ID 2.36mm, $\omega = 0$

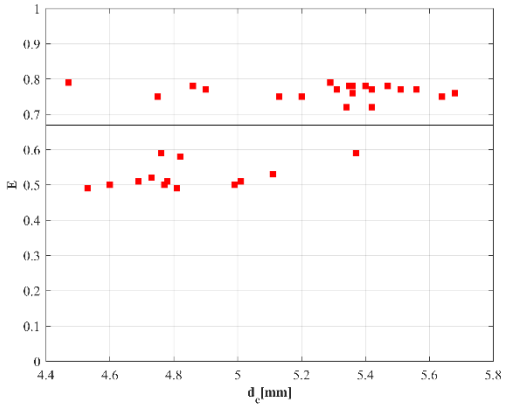

e) ID 2.36mm, $\omega = 0.321/s$

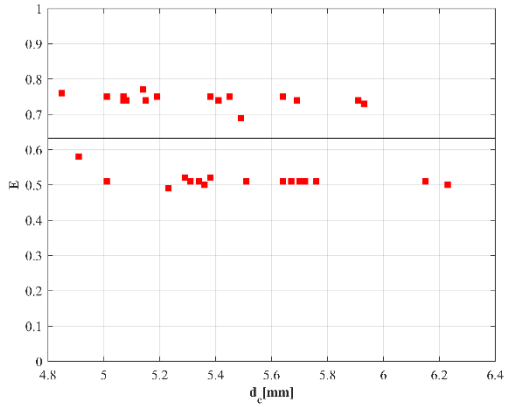

f) ID 2.36mm, $\omega = 0.464/s$

Figure 4-11: Aspect ratio of different-sized bubbles in different flow conditions

Figure 4-11 continued

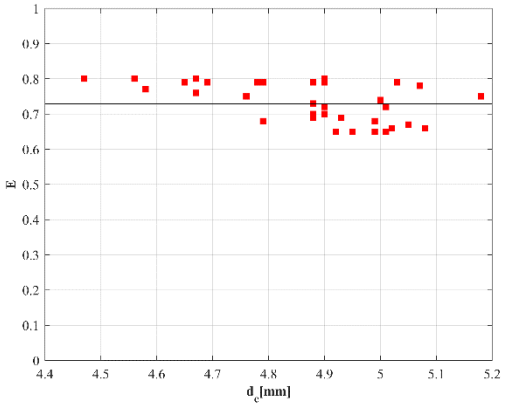

g) ID 3mm, $\omega = 0$

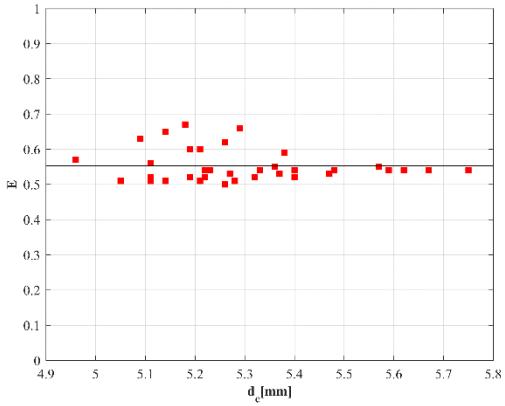

h) ID 3mm, $\omega = 0.321/s$

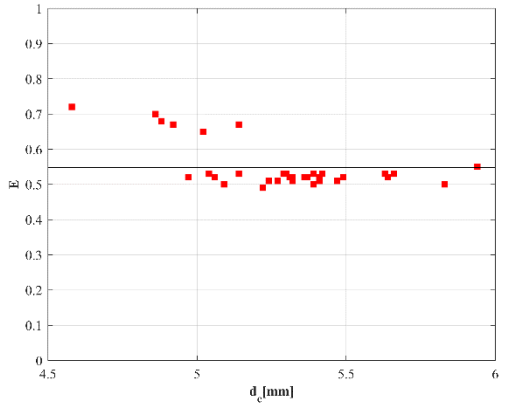

i) ID 3mm, $\omega = 0.464/s$

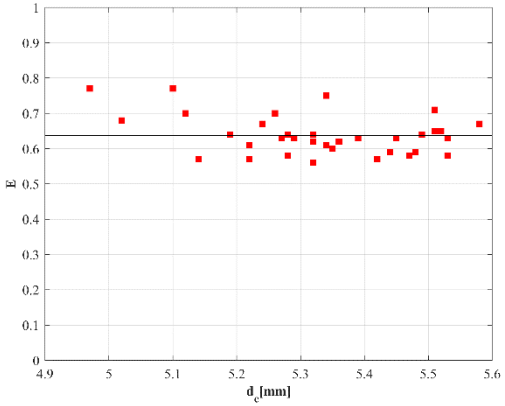

j) ID 3.81mm, $\omega = 0$

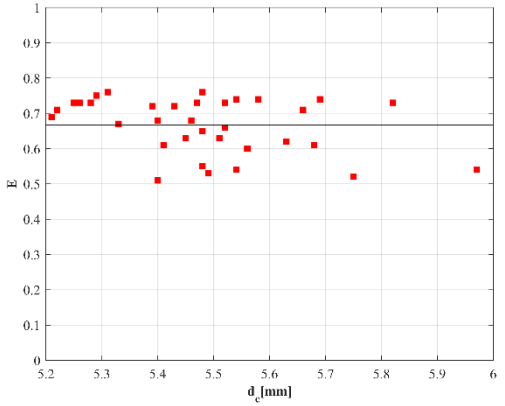

k) ID 3.81mm, $\omega = 0.321/s$

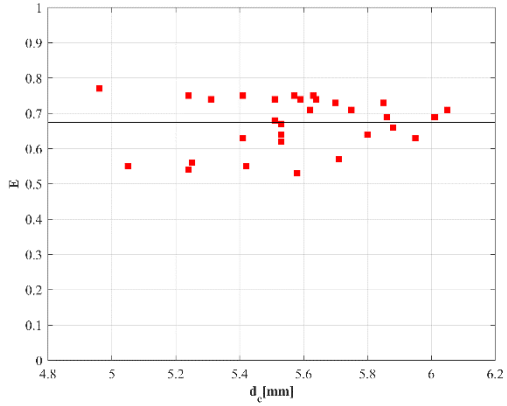

l) ID 3.81mm, $\omega = 0.464/s$

Figure 4-11 continued

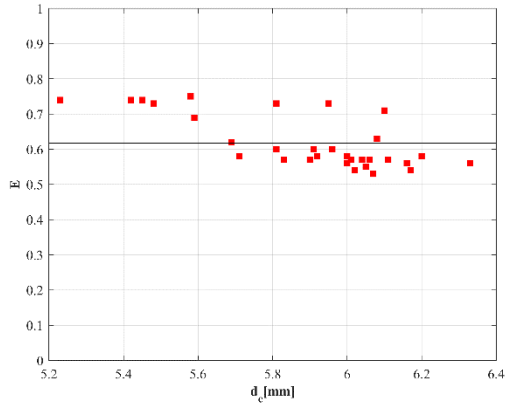

m) ID 4.8mm, $\omega = 0$

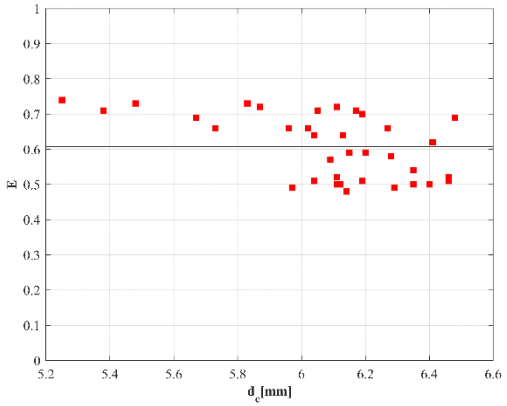

n) ID 4.8mm, $\omega = 0.321/s$

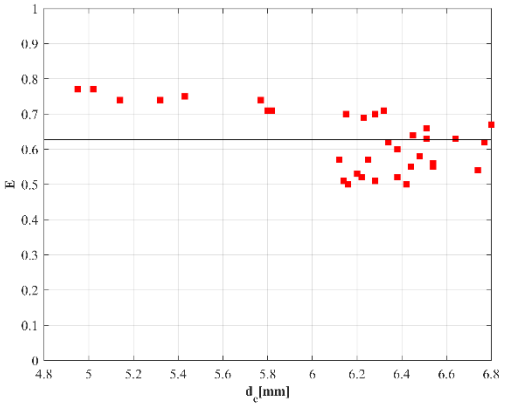

o) ID 4.8mm, $\omega = 0.464/s$

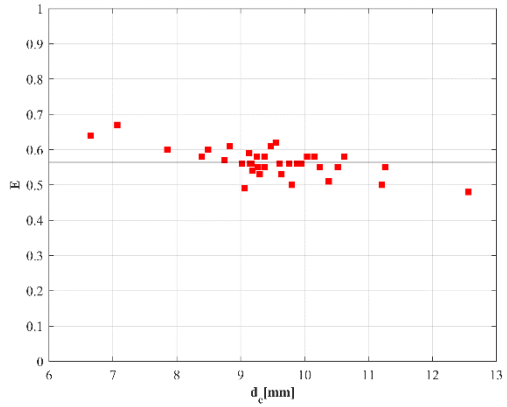

p) Released by Spoon, $\omega = 0$

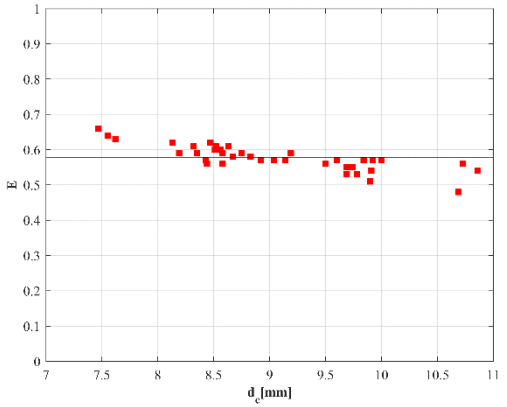

q) Released by Spoon, $\omega = 0.321/s$

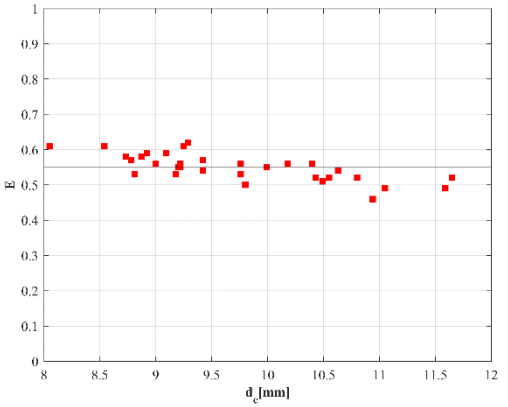

r) Released by Spoon, $\omega = 0.464/s$

Figure 4-11 continued

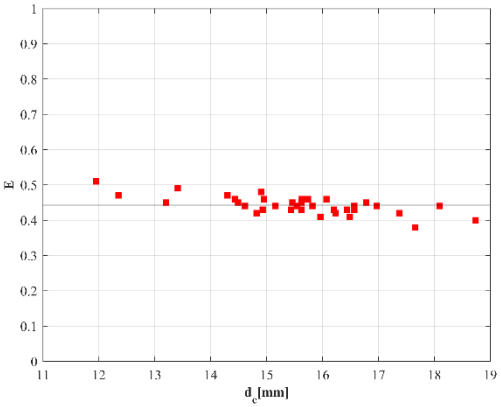

s) Generated by Spoon, $\omega = 0$

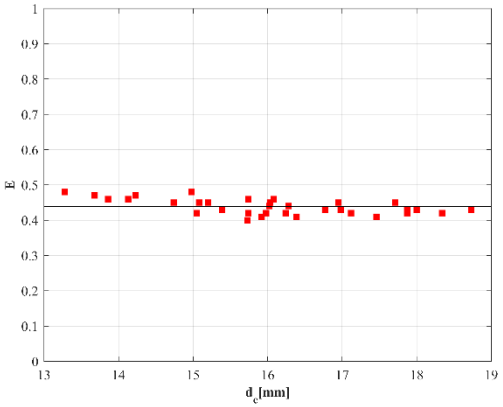

t) Released by Spoon, $\omega = 0.321/s$

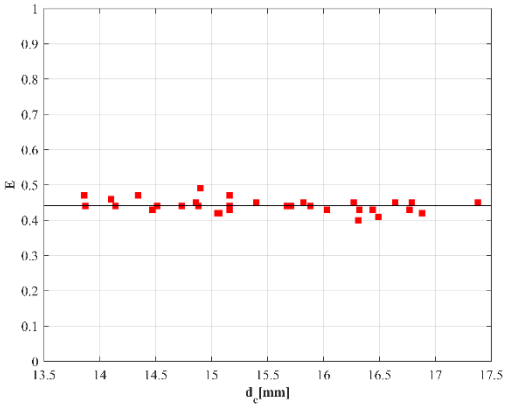

u) Released by Spoon, $\omega = 0.464/s$

4.4 Lift force evaluation

Fig. 4-12 shows two typical bubble trajectories in stagnant water. The bubble in Fig-4-12 (a) rises up with zigzag motion and the net lateral displacement is around 0. The bubble in Fig.4-12 (b) is of similar; however, the bubble migrates to the left side slightly, resulting in negative lateral velocity. This oscillation of bubble trajectory is caused by the Taylor instability, which is not possible to eliminate as the bubble size is large. Thus, the trajectory of each bubble is not always the same and the motion characteristic may vary even though the bubble size is exactly the same. The reasonable approach to tackle this issue is to conduct experiments in the same condition repeatedly and analyze the experiment data statistically. In this experiment, over 30 bubbles with similar size are generated by each needle to analyze their motion characteristics.

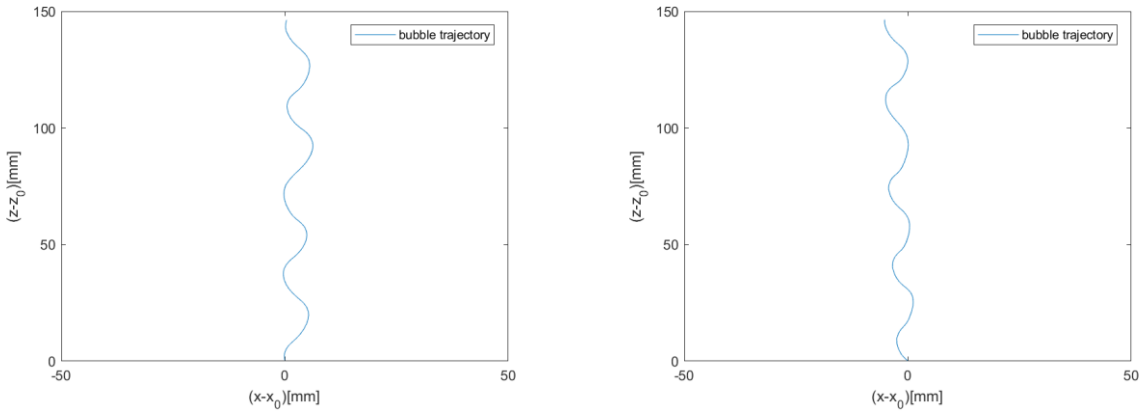

(a) (b)

Figure 4-12: Bubble trajectory varies each time

Bubble lateral movement velocity versus bubble equivalent diameter in stagnant water and two different linear shear fields (0.321/s and 0.464/s) are shown in Fig.4-13. The blue dots represent the experimental data of bubble lateral migration velocity. The red line is the overall velocity trend fitting without physical meaning.

In quiescent water, the lateral velocity of the bubble scatters widely around 0. The largest lateral velocity is within ±10 mm/s for d_e in the range of 2mm and 10mm and increases to ±15 mm/s for d_e larger than 10mm. The trend line almost keeps constant around 0, which means statistically, the bubble dose not preferentially move to either direction in quiescent water. While in the weak

shear flow field with $\omega = 0.321/s$, large bubbles tend to have negative velocity. However, there is no remarkable difference of the velocity for small bubbles compared with the stagnant water case. The trend line indicates that the moving direction of the bubble changes at diameter 7mm. With increasing shear rate magnitude to $\omega = 0.464/s$, the velocity has the similar trend as when in the smaller shear field. However, the trend line shows that the moving direction of the bubbles changes when the bubble equivalent diameter reaches 4mm. This phenomenon agrees with results observed by other researchers that large bubbles tend to migrate to the wall region in downward air-water two-phase flow. The critical diameter for the bubble to change its moving direction is about 5.8mm as observed by Tomiyama et al.(Akio Tomiyama et al., 2002) and 5.7mm as predicted by Hibiki and Ishii's model (Hibiki & Ishii, 2007).

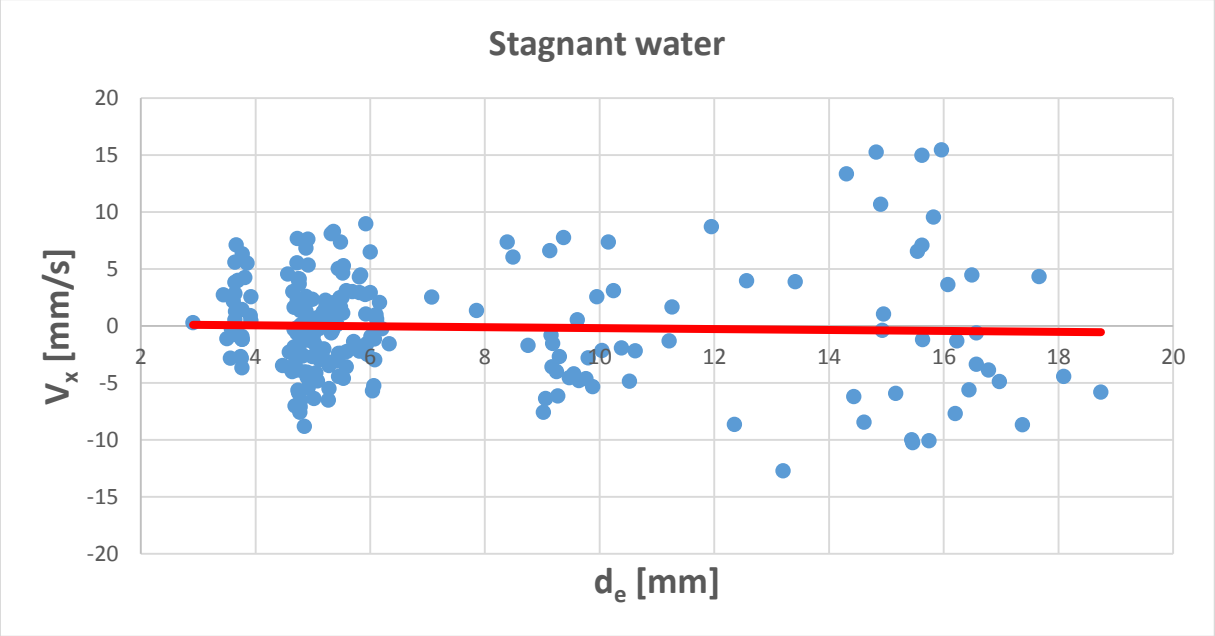

(a)

Figure 4-13: Bubble lateral velocity in stagnant water and shear flow

Figure 4-13 continued

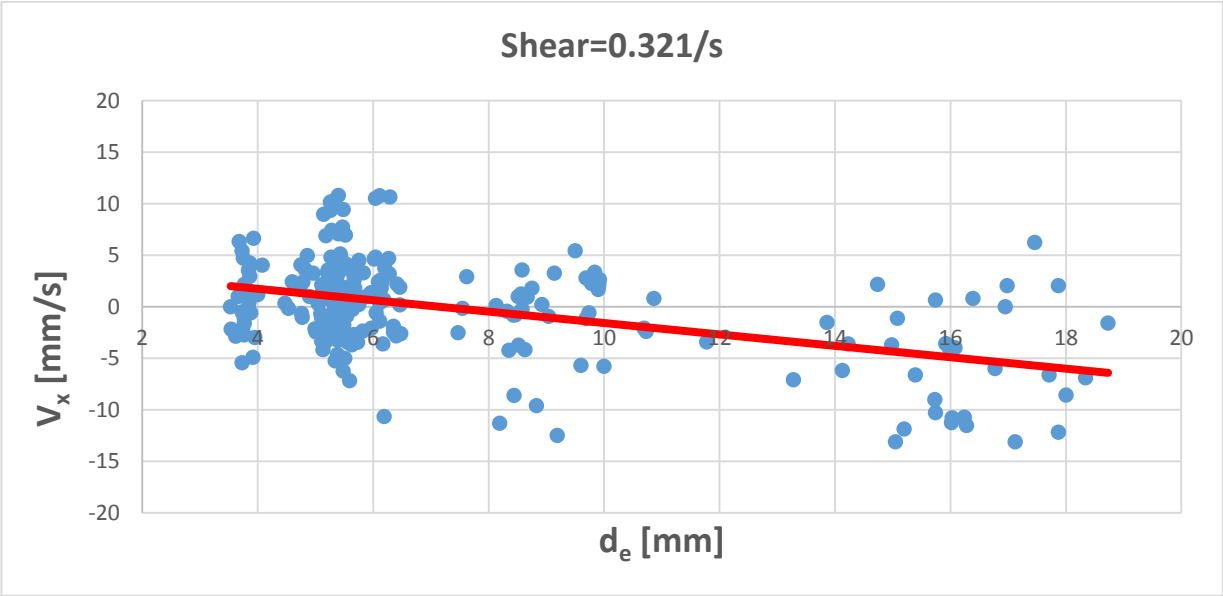

(b)

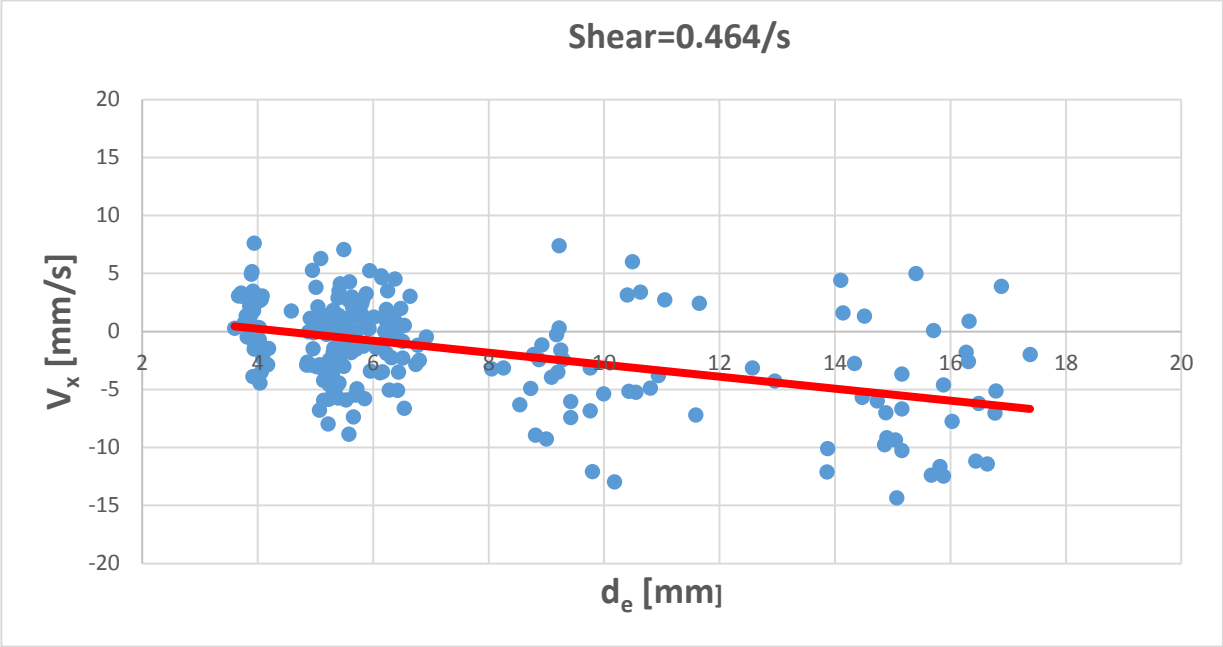

(c)

After obtaining the velocity data of each bubble, the lift coefficient value for each bubble is calculated as discussed in section 3.2.5. Comparison of existing models against experiment data are also presented.

Fig. 4-14 shows the experiment results of lift coefficient value and comparison with existing correlations under the shear rate magnitude $\omega = 0.321/s$.

Large scatter of lift coefficient values is found for bubbles of all sizes investigated in this experiment. The lift coefficient varies from -7 to 7 for intermediate-sized bubbles with d_e from 3mm to 7mm. However, more experiment data fall into the positive value in this region. From statistical viewpoint, it means that the small bubbles tend to have positive lift coefficient. This agrees with all the current models which predict the positive value of the lift coefficient for small bubbles in linear shear flow. Bubbles with d_e over 10mm mostly have negative lift coefficient from -4 to 0, which is between the prediction of Frank et al. model (Frank, Shi, & Burns, 2004) and Auton model (Auton, 1987). According to the trend line of the experimental data, the transition of lift coefficient from positive to negative value occurs at d_e =7mm.

While in the shear condition of $\omega = 0.464/s$ as shown in Fig.4-15, the lift coefficient trend line is below 0, and the extrapolation of the trend line shows that the lift coefficient transition from positive to negative value at d_e =3mm. Bubbles with large diameter also shows negative value of lift coefficient and reach the value of -2 when its equivalent diameter reaches 18mm.

The lift coefficient's dependency on the *Eo* number is shown in Fig.4-14 and Fig.4-16. Similar to the previous case, the data scatters widely for bubbles with *Eo* number from 3 to 50. When *Eo* number is less than 5, the lift coefficient data span the range from -4 to 4. When the *Eo* number increases to 15, the value of lift coefficient mostly shows negative value with some random positive value, which results from the instability of bubble motion.

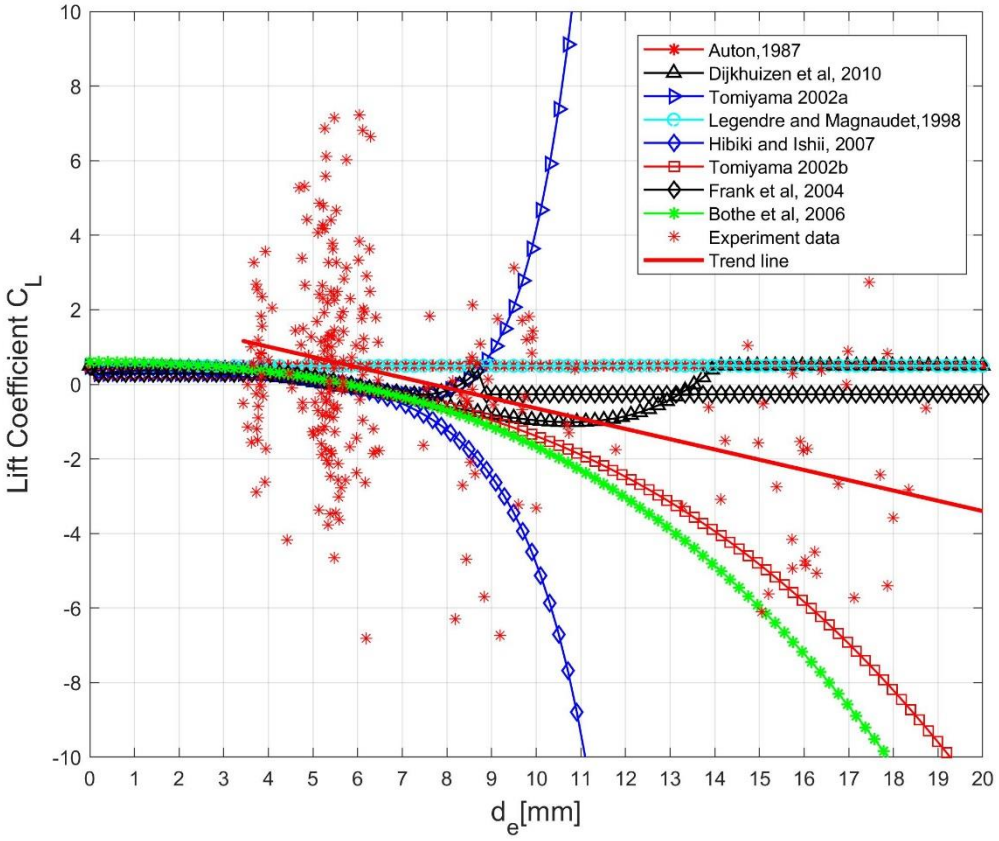

Figure 4-14: Lift coefficient of bubble under shear rate 0.321/s

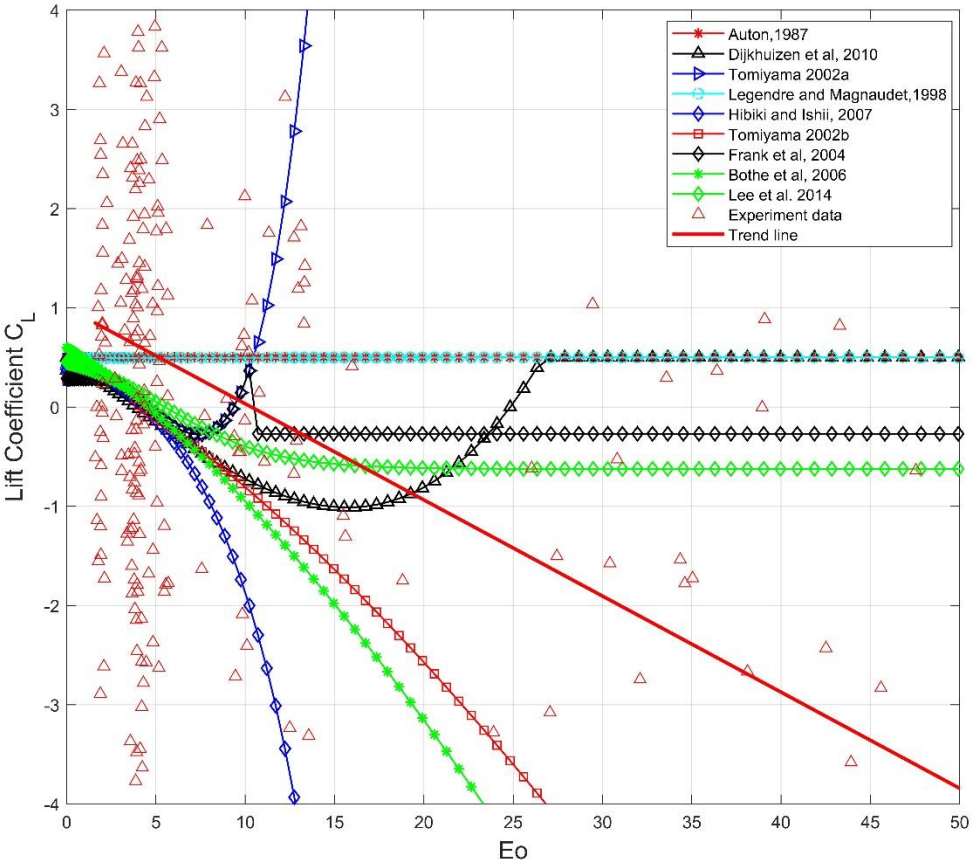

Figure 4-15: Lift coefficient versus *Eo* number under the shear 0.321/s

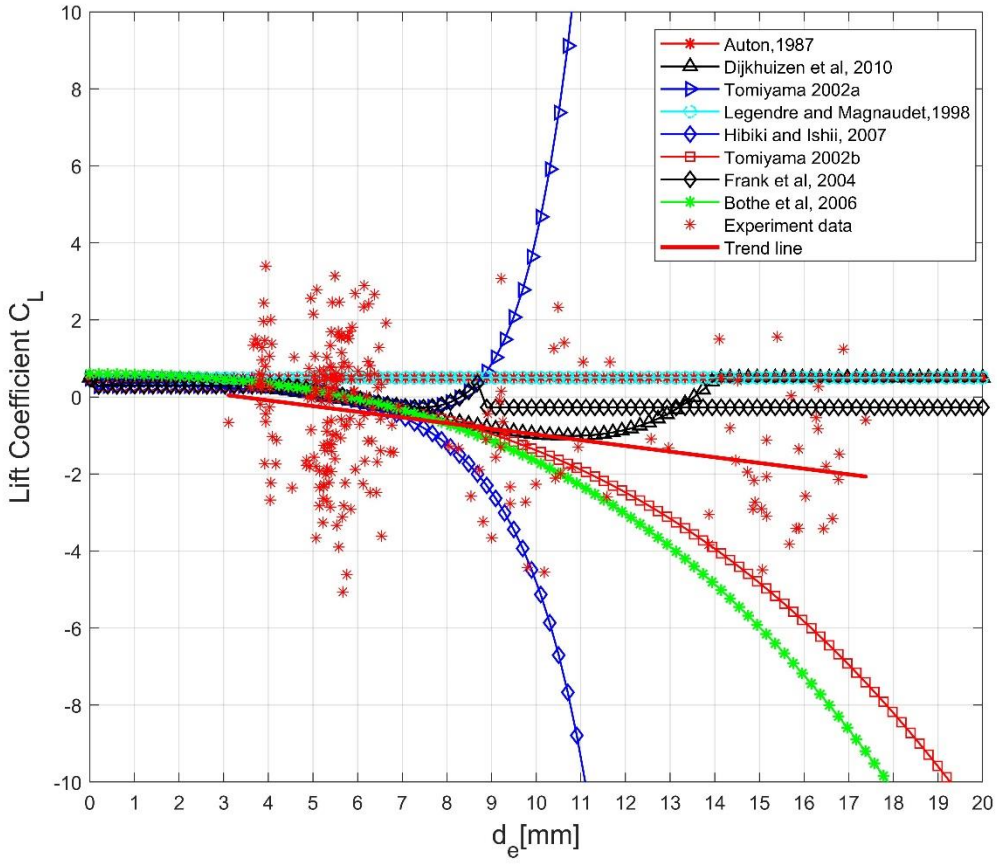

Figure 4-16: Lift coefficient of bubble under shear rate 0.464/s

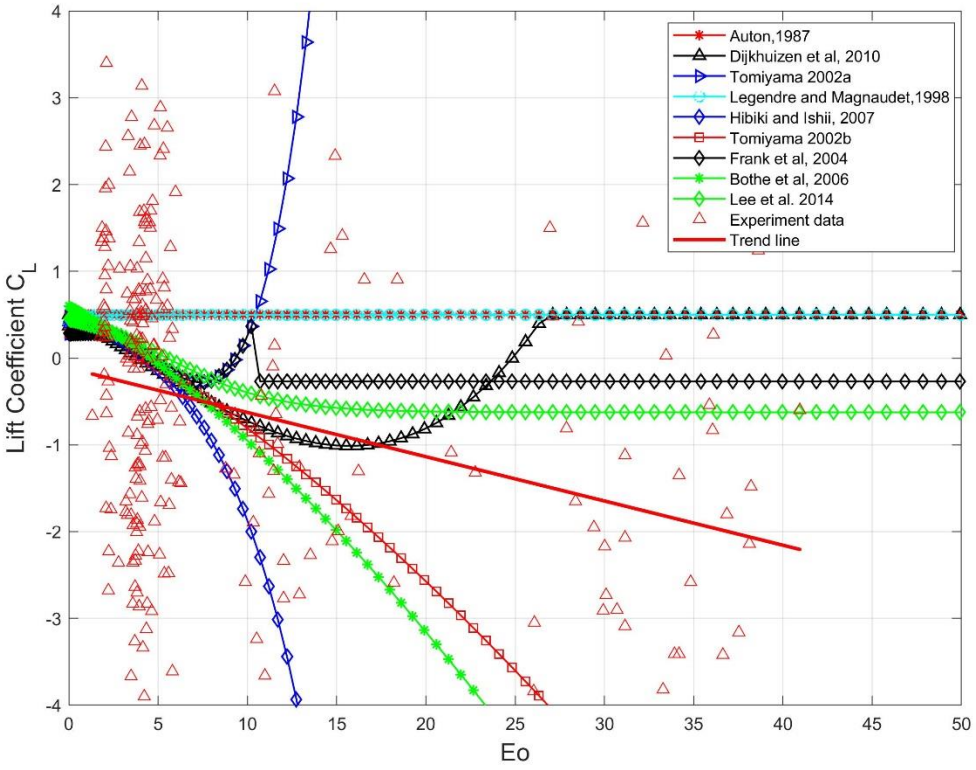

Figure 4-17: Lift coefficient versus *Eo* number under shear rate 0.464/s

In order to better clarify the data, the lift coefficient is calculated for bubbles with similar size. All the bubbles are categorized into several groups first based on their size. The lift coefficient for each group is obtained by taking the average of the lift coefficient values of bubbles within this group. Fig.4-17 and Fig.4-18 show the averaged lift coefficient of the bubble groups. Overall the trend of mean lift coefficient versus bubble size is similar to the linear fitting in Fig 4-13 and Fig.4-15, which decreases with increasing bubble size. However, some discrepancies are found in the averaged trend. The lift coefficient fluctuates between 0.5 to1.5 when the bubble is smaller than 8mm and transits to negative value when bubble is larger than 8mm. A rising trend is found for bubbles with diameter from 9mm to 11mm and then decrease continuously to -2.5 when bubble equivalent diameter reach 16mm. In addition, when shear rate magnitude increase to 0.464/s, lift coefficient increases to 0.75 at the size of 3.5mm. The lift coefficient sign transits from positive to negative earlier at diameter 4mm. Lift coefficient rise up in the range of 5-7mm and 9-11mm,

which is similar with the phenomenon observed in previous case. Afterwards, the lift coefficient declines to -1.75 at d_e =17mm.

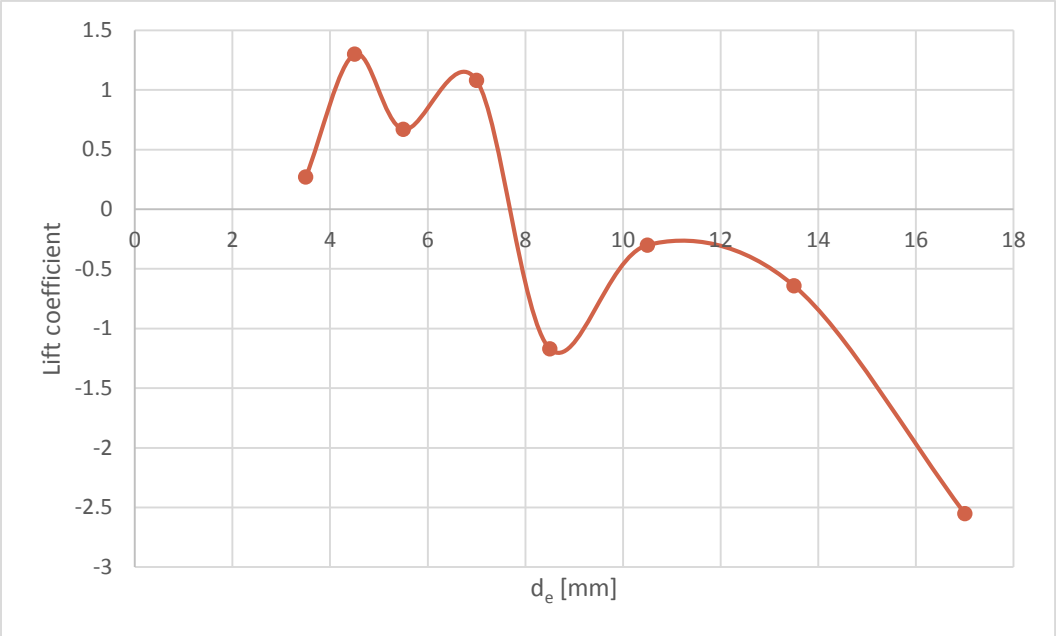

Figure 4-18: Averaged lift coefficient versus bubble size under the shear rate 0.321/s

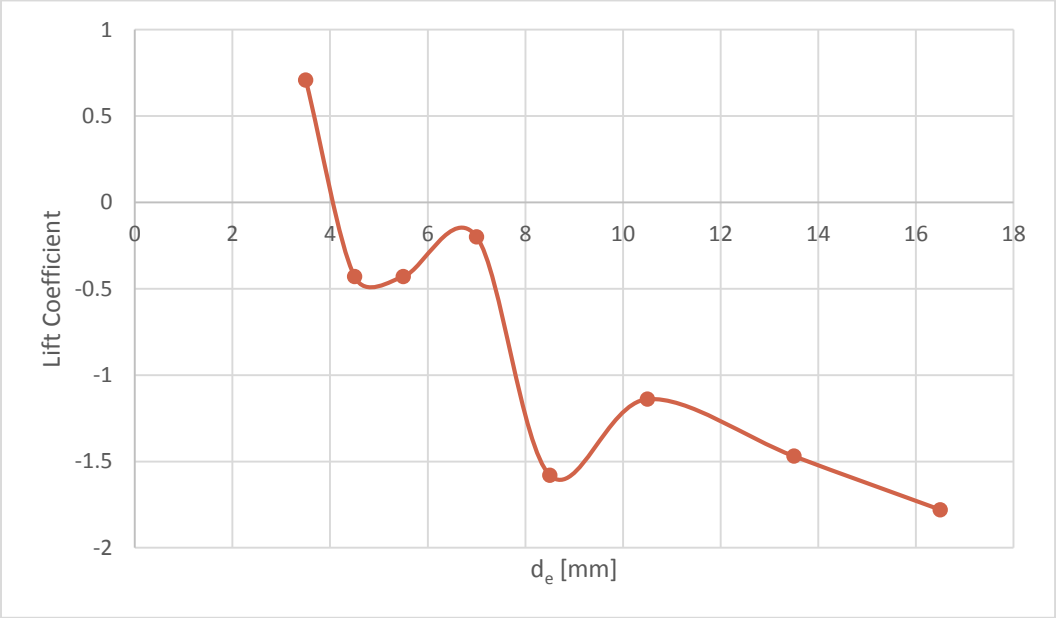

Figure 4-19: Averaged lift coefficient versus bubble size under the shear rate 0.464/s

4.4.1 Comparison with other studies

Auton (Auton, 1987) studied the lift effect on a sphere in weak shear inviscid flow and computation results show a lift value of 0.5 for the sphere. This value is further confirmed by control volume analysis.

Hibiki and Ishii's (Hibiki & Ishii, 2007) suggested that the lift force should relate to the bubble's deformation and introduced a modification factor based on the model developed by Legendre and Magnaude (Legendre & Magnaudet, 1998). The deformation factor would not monotonically decrease with bubble diameter and the lift coefficient should relate only to Reynolds number. With the deformation factor, the new proposed model predicts that the lift coefficient transition from positive to negative value at d_e =5.7mm.

Dijkhuizen et al.'s (Dijkhuizen et al., 2010) simulation results showed that the shear rate has no effect on the lift coefficient while the experiments showed otherwise. The potential reason for this discrepancy is attributed to contamination of the bubble surface, which causes the bubble to behaves like a rigid sphere. In experiments, lift coefficient decreases from positive value to negative value as the bubble diameter increases. Under the shear rate range of 1.0/s and 3.0/s, large lift coefficient value (over than 1) was found for small bubbles in highly viscous liquid. The lift coefficient monotonically decreases with bubble diameter. As the size of the bubble grows, the lift value stays above -1.0 for Eo_H from 0 to 15.

Legendre and Magnaudet (Legendre & Magnaudet, 1998) performed a simulation and found that at low Reynolds number, the lift coefficient associates with the Reynolds number and shear rate. For moderate to high Reynold number, the dependence is very weak, and the lift coefficient approaches asymptotically to the value of 0.5.

Frank et al.(Frank et al., 2004) evaluated Tomiyama's model and noticed lift coefficient would increase sharply to a much higher value.. Thus, the lift coefficient for bubbles with Eo >10 was changed to a constant value of -0.27.

Li et al. (Li, Zhao, et al., 2016) performed experiments in different shear rate magnitude and found that all the bubbles migrate to the same direction and always shows negative lift coefficient. However, in this experiment, small bubbles were found to have positive lift coefficient and transits to negative value with increasing size. It is speculated that the lateral velocity component in the downstream of the curved screen may cause the disagreement.

Experiment data scatters widely in this experiment compared to others. One main reason may be attributed to the low viscosity of the water and high Reynolds number flow condition. In this experiment, water viscosity is 0.00089 compared to 0.018 in Tomiyama's experiment. It needs to be mentioned that the channel's Reynolds number is over 10000, which is significantly larger than that of others' experiments which used highly viscous fluid.

The motion of small bubbles may relate to the high Reynolds number flow and the lift force is significantly reduced by the flow turbulence. As Subash pointed out in his thesis, when channel Reynold number is over 10000, lift force will be reduced due to the turbulence embedded in the flow. The flow field around bubble would be unstable and the behavior of bubble might be affected by the small vortex around. This may explain the velocity distribution of small bubble is similar in both directions. For the large bubble, its shape become more oblate as diameter increases. The non-uniform velocity in different sides make the bubble tilt more to one direction in the whole rising process as shown in Fig. 4-20. The tilt of bubble causes the negative lateral velocity and results in negative lift coefficient. While vortex in the wake of bubble has been suggested as potential reason for the negative lift coefficient, it is not able to verify in this experiment since no measurements is made.

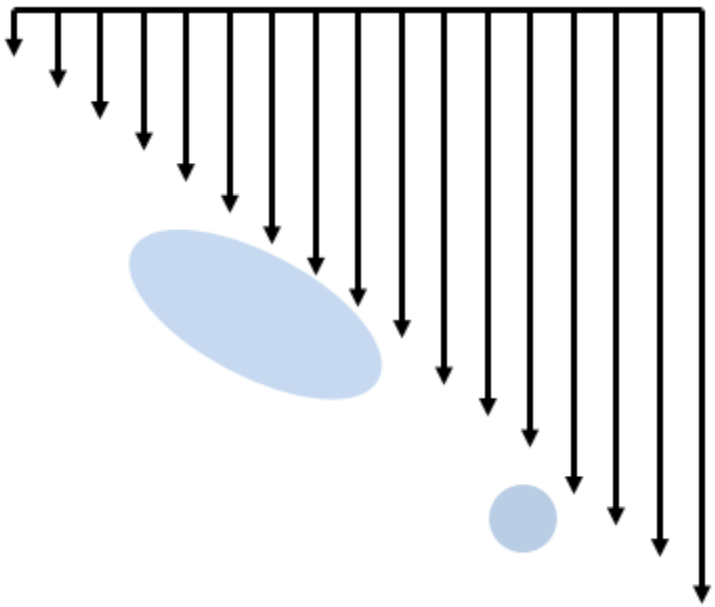

Figure 4-20: Potential reason for the behavior of bubbles in this experiment

In addition, contamination of the water remains a subjective concept to evaluate. The lift force experiments require pure water to eliminate the contamination effects. In review of the literature, some investigators used distilled water while others used deionized water. However, pure water lacks a solid definition. The water used in this experiment and many others is deionized tap water which is considered as pure water based on its low conductivity level. However, it was pointed out by Schenkel et al.(Schenkel & Kitchener, 1958) that water prepared in this way is contaminated by the soluble resin in the filter tanks, which may have unknown effect on the bubble's motion. Because most empirical correlations proposed for the lift coefficient were developed in highly viscous liquid and in small scale space, the wall effect might affect the motion of bubble and thus affects the lift coefficient. Also, the shear rate magnitude in this experiment is relative low. The largest lift coefficient predicted by many correlations is 0.5 for small bubbles. According to existing models, the largest lateral velocity for small bubbles in this experiment would no more than 0.005m/s, which is hard to measure in observation window. In addition, small error in the camera setup configuration would introduce relative large error compared to this small lateral velocity. Thus, requiring a very accurate platform for lift force measurement. Nevertheless, this

experiments still sheds some light on the bubble motion characteristics in stagnant water and weak shear flow and provides more experiment data for further lift force study.

CHAPTER 5. CONCLUSIONS

In this experiment, the lift force is investigated in an air-water system both in stagnant water and weak linear shear flow. The shear rate magnitudes are 0.321/s and 0.464/s. The average flow velocity for these shear rates are -0.10m/s and -0.15m/s, which correspond to the channel's Reynolds number 12449 and 18674, respectively.

The method using a curved mesh screen to generate linear shear flow is evaluated. Although the flow profile shows good linearity, lateral velocity exists in the downstream of the curved screen under the previous design. A honeycomb in the downstream of the screen is recommended to eliminate this lateral velocity component.

In terms of terminal velocity prediction, the model proposed by Tomiyama (A. Tomiyama et al., 2002) has the best prediction of the terminal velocity of bubbles in stagnant water. A tuning factor concerning the asymmetric deformation of bubbles is proposed in this research to best fit the experiment data. The new model is proposed as:

$$V_T = \varepsilon \cdot \frac{\sin^{-1}\sqrt{1-E^2} - E\sqrt{1-E^2}}{1-E^2} \sqrt{\frac{8\sigma}{\rho_L d} E^{4/3} + \frac{\Delta\rho g d}{2\rho_L} \frac{E^{2/3}}{1-E^2}} \tag{5.1}$$

$$\varepsilon = 1.15$$

Scattered bubble aspect ratio was found for bubbles with small size. One reason may be attributed to the pitch-off method for bubble generation, which introduces large initial deformation to the bubbles. In addition, the high Reynolds flow of this research contributes to the wide scatter of lift coefficient data.

For bubbles with diameters from 0-8mm, the upper bound of the aspect ratio decreases with the growth of bubble size. The lower bound of the aspect ratio remains constant around 0.5.

In terms of bubbles with equivalent diameter larger than 8mm. A new aspect ratio correlation is proposed by correlating the Eo number as:

$$E = \frac{1}{1 + 0.239 Eo^{0.475}} \tag{5.2}$$

The model has good agreement with experiment data for bubbles with d_e >8mm .Almost all the experiment data are within ±10% error bound. In addition, the weak shear rate magnitudes of 0.321/s and 0.464/s have no influence on bubble aspect ratio in the present study.

In prospective of bubble oscillation amplitude. Large scatter is found for the small bubbles. The upper bound of oscillation amplitude decreases with equivalent diameter from 2mm to 8mm and increases in the range of 8mm< d_e <20mm. In order to model the oscillation amplitude, it is recommended that more factors should be taken into consideration including the aspect ratio, fluid properties and bubble generation methods.

For the lift force coefficient, experiment data for bubbles with various diameter in low shear rate magnitude flow are provided and comparisons are made with the existing lift coefficient model. According to the experiment data, the weak shear flow does not have remarkable influence on small bubbles in this experiment due to the low viscosity and high Reynolds number flow. The large bubbles show negative lift coefficient under both shear flow conditions. The trend line of the experimental data shows that the lift coefficient transitions from positive to negative value with increasing bubble diameter, which is similar to experiment results obtained in the highly viscous system. However, the shear rate magnitudes in this experiment are relative low, and more data with high shear rate flow in various Reynolds number ranges is suggested in the future.

LIST OF REFERENCE

Adoua, R., Legendre, D., & Magnaudet, J. (2009). Reversal of the lift force on an oblate bubble in a weakly viscous linear shear flow. Journal of Fluid Mechanics, 628, 23–41.

Aoyama, S., Hayashi, K., Hosokawa, S., & Tomiyama, A. (2016). Shapes of ellipsoidal bubbles in infinite stagnant liquids. International Journal of Multiphase Flow, 79, 23–30.

Auton, T. R. (1987). The lift force on a spherical body in a rotational flow. Journal of Fluid Mechanics, 183(1), 199.

Castro, I. P. (1976). Some problems concerning the production of a linear shear flow using curved wire-gauze screens. Journal of Fluid Mechanics, 76(04), 689.

Celata, G. P., Cumo, M., Annibale, F. D., & Di, P. (2006). Effect of gas injection mode and purity of liquid on bubble rising in two-component systems, 31, 37–53.

Chen, Y.-K., Milos, F. S., & Kotansky, D. R. (1966). The use of honeycomb for shear flow generation. AIAA Journal, 4(8), 1490–1491.

Clift, R., Grace, J. R., & Weber, M. E. (2005). Bubbles, drops, and particles. Courier Corporation.

Dijkhuizen, W., van Sint Annaland, M., & Kuipers, J. A. M. (2010). Numerical and experimental investigation of the lift force on single bubbles. Chemical Engineering Science, 65(3), 1274–1287.

Dunn, W., & Tavoularis, S. (2007). The use of curved screens for generating uniform shear at low Reynolds numbers. Experiments in Fluids, 42(2), 281–290.

Elder, J. . (1959). Steady flow through non-uniform gauzes of arbitrary shape. Journal of Fluid Mechanics, 5(03), 355.

Fascination, I. N., & Fluid, O. F. (1998). In Facination of Fluid Dynamics.

Feng, J., & Bolotnov, I. A. (2017). Interfacial force study on a single bubble in laminar and turbulent flows. Nuclear Engineering and Design, 313, 345–360.

Frank, T., Shi, J., & Burns, A. D. (2004). Validation of Eulerian multiphase flow models for nuclear safety application. In Proceeding of the Third International Symposium on Two-Phase Modelling and Experimentation, Pisa, Italy. Citeseer.

Hibiki, T., & Ishii, M. (2007). Lift force in bubbly flow systems. Chemical Engineering Science, 62(22), 6457–6474.

Ishii, M., & Chawla, T. C. (1979). Local drag laws in dispersed two-phase flow. Nasa Sti/Recon

Technical Report N, 80.

Ishii, M., & Hibiki, T. (2010). Thermo-fluid dynamics of two-phase flow. Springer Science & Business Media.

Lamb, H. (1993). Hydrodynamics. Cambridge university press.

Lee, J. Y., & Choi, Y. S. (n.d.). Lift Force of Large Bubble in High Reynolds Condition, 346–357.

Legendre, D., & Magnaudet, J. (1998). The lift force on a spherical bubble in a viscous linear shear flow. Journal of Fluid Mechanics, 368, 81–126.

Li, Z., Song, X., Jiang, S., & Ishii, M. (2016). The lateral migration of relative large bubble in simple shear flow in water. Experimental Thermal and Fluid Science, 77(Supplement C), 144–158.

Li, Z., Zhao, Y., Song, X., Yu, H., Jiang, S., & Ishii, M. (2016). Experimental investigation of single small bubble motion in linear shear flow in water. Nuclear Engineering and Design, 305(Supplement C), 334–346.

Lucas, D., & Tomiyama, A. (2011). On the role of the lateral lift force in poly-dispersed bubbly flows. International Journal of Multiphase Flow, 37(9), 1178–1190.

Maldonado, M., Quinn, J. J., Gomez, C. O., & Finch, J. A. (2013). An experimental study examining the relationship between bubble shape and rise velocity. Chemical Engineering Science, 98, 7–11.

Mendelson, H. D. (1967). The prediction of bubble terminal velocities from wave theory. AIChE Journal, 13(2), 250–253.

Okawa, T., Tanaka, T., Kataoka, I., & Mori, M. (2003). Temperature effect on single bubble rise characteristics in stagnant distilled water. International Journal of Heat and Mass Transfer, 46(5), 903–913.

Owen, P. R., & Zienkiewicz, H. K. (1957). The production of uniform shear flow in a wind tunnel. Journal of Fluid Mechanics, 2(6), 521–531.

Peebles, F. N. (1953). Studies on the motion of gas bubbles in liquid. Chem. Eng. Prog., 49(2), 88–97.

Peters, F., & Els, C. (2012). An experimental study on slow and fast bubbles in tap water. Chemical Engineering Science, 82, 194–199.

Raffel, M., Willert, C. E., Scarano, F., Kähler, C. J., Wereley, S. T., & Kompenhans, J. (2018). Particle image velocimetry: a practical guide. Springer.

Saffman, P. G. (1965). The lift on a s m a l l sphere in a slow shear f l o w. Fluid Mechanics, 22, 385–400.

Schenkel, J. H., & Kitchener, J. A. (1958). Contamination of surfaces by conductivity water from ion-exchange resins. Nature, 182(4628), 131.

Schiller, L., & Naumann, Z. (1933). A drag coefficient correlation. Z.Ver.Deutsch.Ing, 77(13–14), 318–320.

Serizawa, A., Kataoka, I., & Michiyoshi, I. (1975). Turbulence structure of air-water bubbly flow-II. local properties. International Journal of Multiphase Flow, 2(3), 235–246.

Sugihara, K., Sanada, T., Shirota, M., & Watanabe, M. (2007). Behavior of single rising bubbles in superpurified water. Kagaku Kogaku Ronbunshu, 33(5), 402–408.

Taylor, T. D., & Acrivos, A. (1964). On the deformation and drag of a falling viscous drop at low Reynolds number. Journal of Fluid Mechanics, 18(3), 466–476.

Tomiyama, A., Celata, G. P., Hosokawa, S., & Yoshida, S. (2002). Terminal velocity of single bubbles in surface tension force dominant regime. International Journal of Multiphase Flow, 28(9), 1497–1519.

TOMIYAMA, A., KATAOKA, I., ZUN, I., & SAKAGUCHI, T. (1998). Drag Coefficients of Single Bubbles under Normal and Micro Gravity Conditions. JSME International Journal Series B, 41(2), 472–479.

Tomiyama, A., Tamai, H., Zun, I., & Hosokawa, S. (2002). Transverse migration of single bubbles in simple shear flows. Chemical Engineering Science, 57(11), 1849–1858.

Tsuge, H., & Hibino, S. I. (1977). The Onset Conditions of Oscillatory Motion of Single Gas Bubbles Rising in Various Liquids. Journal of Chemical Engineering of Japan, 10(1), 66–68.

Turner, J. T. (1969). A computational method for the flow through non-uniform gauzes: the general two-dimensional case. Journal of Fluid Mechanics, 36(02), 367.

Usui, K., & Sato, K. (1989). Vertically downward two-phase flow, (I) void distribution and average void fraction. Journal of Nuclear Science and Technology, 26(7), 670–680.

Wallis, G. B. (1974). The terminal speed of single drops or bubbles in an infinite medium. International Journal of Multiphase Flow, 1(4), 491–511.

Wang, S. K., Lee, S. J., Jones, O. C., & Lahey, R. T. (1987). 3-D turbulence structure and phase distribution measurements in bubbly two-phase flows. International Journal of Multiphase Flow, 13(3), 327–343.

Wellek, R. M., Agrawal, A. K., & Skelland, A. H. P. (1966). Shape of liquid drops moving in liquid media. AIChE Journal, 12(5), 854–862.

Wu, M., & Gharib, M. (2002). Experimental studies on the shape and path of small air bubbles rising in clean water. Physics of Fluids, 14(7).

Ẑun, I. (1980). The transverse migration of bubbles influenced by walls in vertical bubbly flow. International Journal of Multiphase Flow, 6(6), 583–588.